Earth System
Science
Data

Improving the usability of the Multi-angle Imaging SpectroRadiometer (MISR) L1B2 Georectified Radiance Product (2000–present) in land surface applications

Michel M. Verstraete[1], Linda A. Hunt[2], and Veljko M. Jovanovic[3]

[1]Global Change Institute (GCI), University of the Witwatersrand, Braamfontein, Republic of South Africa
[2]Science Systems and Applications, Inc. (SSAI), Hampton, VA 23666-5845, USA
[3]NASA Jet Propulsion Laboratory (JPL), Pasadena, CA 91109, USA

Correspondence: Michel M. Verstraete (michel.verstraete@wits.ac.za, mmverstraete@gmail.com)

Abstract. The Multi-angle Imaging SpectroRadiometer (MISR) instrument on NASA's Terra platform has been acquiring global measurements of the spectrodirectional reflectance of the Earth since 24 February 2000 and is still operational as of this writing. The primary radiometric data product generated by this instrument is known as the Level 1B2 (L1B2) Georectified Radiance Product (GRP): it contains the 36 radiometric measurements acquired by the instrument's nine cameras, each observing the planet in four spectral bands. The product version described here is projected on a digital elevation model and is available from the NASA Langley Atmospheric Science Data Center (ASDC; http://doi.org/10.5067/Terra/MISR/MI1B2T_L1.003; Jovanovic et al., 1999). The MISR instrument is highly reliable. Nevertheless, its onboard computer occasionally becomes overwhelmed by the number of raw observations coming from the cameras' focal planes, especially when switching into or out of LOCAL MODE acquisitions that are often requested in conjunction with field campaigns. Whenever this occurs, one or more lines of data are dropped while the computer resets and readies itself for accepting new data. Although this type of data loss is minuscule compared to the total number of measurements acquired and is marginal for atmospheric studies dealing with large areas and long periods of time, this outcome can be crippling for land surface studies that focus on the detailed analysis of particular scenes at specific times. This paper describes the problem, reports on the prevalence of missing data, proposes a practical solution to optimally estimate the values of the missing data and provides evidence of the performance of the algorithm through specific examples in southern Africa. The software to process MISR L1B2 GRP data products as described here is openly available to the community from the GitHub website (https://github.com/mmverstraete or https://doi.org/10.5281/zenodo.3519988). Two additional sets of resources are also made available on the research data repository of GFZ Data Services in conjunction with this paper. The first set (A; Verstraete et al., 2020, https://doi.org/10.5880/fidgeo.2020.012) includes five items: (A1) a compressed archive (`L1B2_Out.zip`) containing all intermediary, final and ancillary outputs created while generating the figures of this paper; (A2) a user manual (`L1B2_Out.pdf`) describing how to install, uncompress and explore those files; (A3) an additional compressed archive (`L1B2_Suppl.zip`) containing a similar set of results, only for eight other sites, spanning a much wider range of geographical, climatic and ecological conditions; (A4) a companion user manual (`L1B2_Suppl.pdf`) describing how to install, uncompress and explore those additional files; and (A5) a separate input MISR data archive (`L1B2_input_68050.zip`) for PATH 168, ORBIT 68050. This latter archive is usable with the second set (B; Verstraete and Vogt, 2020; https://doi.org/10.5880/fidgeo.2020.011), which includes (B1) a stand-alone, self-contained, executable version of the L1B2 correction codes (`L1B2_Soft_Win.zip`) that uses the IDL Virtual Machine technology and does not require a paid IDL license as well as (B2) a user manual (`L1B2_Soft_Win.pdf`) that explains how to install, uncompress and use this software.

1 Introduction

The Multi-angle Imaging SpectroRadiometer (MISR) is one of the five Earth-observing instruments hosted on the NASA Terra platform, launched into a sun-synchronous low-Earth orbit on 18 December 1999 (altitude: 713 km; equatorial crossing time: 10:30 local time). The orbit of Terra is precisely maintained so that, after completing 233 revolutions, the satellite observes the same locations on Earth again from the same directions; this cycle takes 16 days, so the satellite performs 14.6 orbits per day. Each of those systematically repeating tracks is called a PATH. MISR features nine cameras pointing forward, nadir and aft in relation to the platform at various bore angles (DF: 70.3°; CF: 60.2°; BF: 45.7°; AF: 26.2°; AN: 0.1°; AA: 26.2°; BA: 45.7°; CA: 60.2°; and DA: 70.6°). Each camera is equipped to acquire data in four spectral bands of 20–40 nm full width at half height – blue (446.4 nm), green (557.5 nm), red (671.7 nm) and near-infrared (866.4 nm) – for a total of 36 data channels. MISR became operational on 24 February 2000 and is still collecting data as of this writing. This instrument has been extensively described in the literature (Diner et al., 1989, 1998, 1999a, 2002, 2005) and more recently in a special issue of the MDPI journal *Remote Sensing* dedicated to that instrument (see https://www.mdpi.com/journal/remotesensing/special_issues/misr_rs, last access: 29 May 2020).

The primary mission of the MISR instrument is to acquire reflected radiance measurements while overflying the day side of the Earth for the purpose of quantitatively characterizing the state and evolution of the Earth's atmosphere (clouds and aerosols) and surface (vegetation and soils over land or water properties over oceans), including the cryosphere (glaciers, ice caps and sea ice). Specifically, its combined multiangular and multispectral capability has proven very useful in investigating land surface processes, especially when coupled with in situ observations (field campaigns) or other sources of environmental data (e.g., Armston et al., 2007; Chopping et al., 2008; Pisek and Chen, 2009; Wei and Fang, 2016; Liu et al., 2018; Mahlangu et al., 2018; Van den Hoof et al., 2018). All MISR data products are archived at and distributed from the NASA Atmospheric Science Data Center (ASDC) in Hampton, Virginia.

It turns out that the Level 1B2 (L1B2) Georectified Radiance Product (GRP) data product exhibits a variable number of missing values, especially over continental areas. For reasons that will be explored in the next section, this issue may happen randomly anywhere and at any time, but it occurs mostly whenever the instrument is switched between its default GLOBAL MODE and the occasional LOCAL MODE. These events often perturb most spectral bands of a camera and more than one camera. Missing lines are detected as part of Level 1 processing and marked with the appropriate code indicating that measurements were lost. All data prod-

ucts subsequently derived from these sources are of course unavailable too.

These events imply significant consequences for land surface products, which often rely on multiple spectral bands, e.g., vegetation indices, or on the whole range of cameras and bands, e.g., in assessing advanced products like surface albedo and the fraction of absorbed photosynthetically active radiation (FAPAR), for instance. Such data loss can be crippling to the investigation, especially if it occurs systematically in space and time or at the very place and time when a field campaign is taking place.

A procedure is thus required to minimize the number of missing values in MISR data files and to maximize the spatial coverage of derived land surface products. The purpose of this paper is to report on the prevalence of this problem, to describe a proposed solution and to show the performance of the suggested approach through concrete examples.

Section 2 discusses the origin and distribution of missing data in MISR L1B2 GRP data files. Section 3 describes the various input data files required as well as the proposed algorithm, while Sect. 4 exhibits concrete results. Finally, Sect. 5 explores the effectiveness of that algorithm.

2 Problem statement and motivation

The primary MISR data, from which all surface products are derived, are the L1B2 Georectified Radiance Products (GRPs), which contain in particular the terrain-projected product of interest here. The latter provides calibrated multiangular and multispectral observations of the planetary reflectance measured by the instrument at the nominal "top of the atmosphere" (ToA), projected to a space-oblique Mercator (SOM) grid and georeferenced and corrected for terrain relief effects using a digital elevation model.

2.1 Global and Local modes of operation

L1B2 GRP radiance measurements in each of the nine cameras and four spectral bands are acquired by the instrument at the native spatial resolution of 275 m (across-track, for the eight off-nadir-pointing cameras) or 250 m (across-track, for the nadir-pointing camera), although the latter is subsequently resampled to 275 m to provide the same sampling in all full-resolution data channels (Jovanovic et al., 1999; Bull et al., 2011). The resulting instrument-wide rate of data acquisition exceeds the downlink bandpass allotted to MISR by the Terra platform. To fit that constraint in its default GLOBAL MODE, 12 of those 36 data channels (the four spectral bands of the nadir-pointing camera and the red spectral band of the eight off-nadir-pointing cameras) are transmitted to the ground segment at the full native spatial resolution, while the remaining 24 data channels (i.e., the nonred spectral bands of the off-nadir-pointing cameras) are averaged

on 4 pixel × 4 pixel areas onboard the platform. This process achieves a 16 : 1 compression ratio in those data channels and thus delivers data at the reduced spatial resolution of 1100 m. As a result, all standard MISR land products available from NASA are generated at this lower spatial resolution.

Upon request, the MISR instrument can also be operated in LOCAL MODE (LM). When this mode is activated, each camera is allowed to transmit data in turn at the native spatial resolution of the detectors in all four spectral bands for a limited period of time, corresponding to a scene of about 300 km along-track. LM acquisitions occur mostly over continental areas and are requested in three broad categories of cases: (1) to systematically assess the performance of the instrument through vicarious calibration exercises over fixed, well-documented sites and throughout the mission; (2) to support field campaigns over the areas of interest and for the duration of those exercises; or (3) to promote thematic studies, for instance over polluted urban areas, or to monitor a dynamically evolving region. About 100 sites have been identified for LM acquisition over the first 20 years of operation of MISR, with periods of observation ranging from a few weeks to the entire duration of the mission. The number of LM acquisitions per ORBIT is a mission design constraint as each one requires the specific reprogramming of the instrument and leads to larger data transfers to the ground segment. In practice, only one LM acquisition is allowed per ORBIT on an operational basis. At the time of writing (mid-March 2020), LOCAL MODE acquisitions were undertaken roughly 3 to 8 times a day (out of 14 opportunities). The ASDC maintains a table, updated daily, reporting on the success of LM acquisitions (see https://l0dup05.larc.nasa.gov/public/cgi-bin/DUE/ecs_LocalMode_history_PR.cgi, last access: 29 May 2020).

During the initial preprocessing phase, the original analog radiance measurements acquired by the instrument's cameras are converted to 16-bit unsigned integers, where the first (most significant) 14 bits contain the scaled radiance itself, and the last 2 bits constitute the radiometric data quality indicator (RDQI), an indicator of the estimated reliability of the data item. The floating point radiance is obtained by unpacking those last 2 bits and multiplying the resulting value by the scale factor that is included in the data file. There is also a one-to-one relationship between the radiance and the nondimensional bidirectional reflectance factor (denoted Brf in this paper; p. 73 in Bull et al., 2011):

$$\text{Brf} = [(\pi \times D^2)/(W \times \cos\theta_s)] \times \text{Rad}, \quad (1)$$

where D is the approximate distance in astronomical units between the center of the Earth and the center of the Sun at the time MISR observes the first valid (nonfill) pixel in the swath (this information does not vary with spectral bands but is replicated across bands for convenience; p. 60 in Bull et al., 2011), $W = E_0^{\text{std}}(b)$ is the band-specific weighted standardized solar irradiance (W m^{-2} μm^{-1}; Bull et al., 2011, p. 65–68), θ_s is the solar zenith angle and Rad stands for the floating point radiance value (W m^{-2} sr^{-1} μm^{-1}).

Table 1. Meaning of the 2-bit RDQI values in L1B2 GRP data files.

Decimal	Binary	Meaning
0	00	Within specifications ("good")
1	01	Reduced accuracy ("fair")
2	10	Not usable for science ("poor")
3	11	Unusable for any purpose ("missing")

The onboard computer that manages the measurements and performs the GLOBAL MODE (GM) spatial averaging may occasionally be overwhelmed by the high data acquisition rate. This appears to occur randomly at a low but unpredictable frequency. However, the number of missing data values increases by at least an order of magnitude whenever the instrument is switched from the default GLOBAL MODE to LOCAL MODE (LM) and conversely. A procedure is thus required to replace those missing values, and it must be designed to work effectively everywhere and all the time.

2.2 Detecting missing values

The first step in this investigation consists of documenting the prevalence of this problem, which implies distinguishing missing values due to this onboard computer glitch from other causes. As explained above, radiance values are represented in the L1B2 GRP data files by 16-bit unsigned integers, where the last 2 bits are the RDQI. Table 1 describes the meaning attached to the values of this quality indicator (Bull et al., 2011, p. 71).

The algorithm used to assign the RDQI value to each pixel is described in detail in Jovanovic et al. (1999). Practical experience with this data product indicates that an RDQI value of 1 refers to either a minor increase in the uncertainty of the radiance value or a possible slight misregistration of the pixel, while a value of 2 indicates a larger radiance uncertainty, for instance in the presence of sun glint reflected from a still water surface. An RDQI value of 3 can be assigned to a terrain-projected L1B2 GRP value in four different cases, and the radiance value itself indicates why those values are unusable. CE1

CE1: OK

1. When the location of a pixel on the ground is obscured by topography for the specified camera, an issue that mostly affects off-nadir-pointing cameras, its value is coded as the unsigned 16-bit integer 65 511, equivalent to a scaled 14-bit radiance of 16 377.

2. When the location of a pixel on the ground lies outside of the swath width of the camera, which occurs on the western and eastern edge of each BLOCK, its value is coded as the unsigned 16-bit integer 65 515, equivalent to a scaled 14-bit radiance of 16 378.

https://doi.org/10.5194/essd-12-1-2020

Figure 1. Example of missing lines (in this case two consecutive lines) in the L1B2 terrain-projected LOCAL MODE bidirectional reflectance factor data for the blue spectral band of the DF camera for PATH 168, ORBIT 68 050 and BLOCK 110, covering an area located in eastern South Africa. The linear gray scale, shown on the right side of the frame, assigns Brf values of 0 to black and Brf values of 0.35 or higher to white. The black spots on the western side of the map are due to pixels that are not observed at this slanted view angle due to the local topography. North is approximately towards the top of the image. The total size of the BLOCK area is 563.2 km across-track (roughly west–east) by 140.8 km along-track (roughly north–south), while the parallelogram-shaped ground area inside the BLOCK is about 380 km across-track.

3. When the location of a pixel at the Earth's surface belongs to a BLOCK covering an ocean region only, its value is coded as the unsigned 16-bit integer 65 519, equivalent to a scaled 14-bit radiance of 16 379.

4. When the radiance estimated for a location is deemed unusable for a reason other than orography, edge or ocean, its value is coded as the unsigned 16-bit integer 65 523, equivalent to a scaled 14-bit radiance of 16 380 (this is a "missing" value in the context of this paper).

Consequently, the RDQI is an indicator of missing values in the sense described earlier only if it is associated with an unsigned 16-bit radiance value of 65 523.

Figure 1 exhibits a simple example: in this case, a couple of lines have been dropped from the blue spectral band in BLOCK 110 of the DF camera in the LOCAL MODE bidirectional reflectance factor data file. In this context, a BLOCK is a segment of data that covers a ground area of about 563.2 km across-track by 140.8 km along-track, which contains usable data over roughly 380 km across-track as well as fill data on both edges. Figure 2 of Verstraete et al. (2020) shows the geographical location of this BLOCK in southern Africa. These missing lines tend to occur simultaneously in all spectral bands, but because the spectral detectors are located next to each other on the focal plane of each camera, the corresponding locations of these missing values on the ground, and therefore in the images, are slightly displaced. As a result, products that combine multiple spectral bands from the same camera inherit all missing lines from each of the individual bands. And of course, a missing line in the LOCAL MODE data also implies a missing line in the corresponding GLOBAL MODE data with an added side effect: the missing lines in the nonred spectral channels of the off-nadir cameras show up with a width of 1100 m (or multiples thereof). Figure 2 exhibits the RGB image for the GLOBAL MODE

acquisition corresponding to the case shown in Fig. 1 (top frame) as well as the corresponding map of the NIR spectral band for the same camera.

2.3 Counting missing and poor values

An examination of the MISR L1B2 GRP terrain-projected GLOBAL MODE (GM) radiance files for BLOCKs 110 to 113 of PATHs 168 to 170 from the start of the mission onwards revealed that millions of pixel values went missing (RDQI of 3 and scaled radiance of 16 380) in GLOBAL as well as LOCAL MODE acquisitions.

For instance, Fig. 3 exhibits the logarithm in base 10 of the number of missing pixels in the four spectral bands of the nine cameras for BLOCK 110 of all available ORBITs of PATH 168 between 24 March 2000 and 23 December 2018: a total of 2 143 033 pixel values went missing. LOCAL MODE data were briefly acquired at the start of the MISR mission for the Skukuza flux tower site located in Kruger National Park in South Africa in support of the Safari-2000 campaign. This site, which covers an area roughly equivalent to BLOCKs 110 and 111, has subsequently been systematically acquired from December 2009 onward. The net effect of switching from GLOBAL to LOCAL MODE (and back) on the number of missing values is clearly visible in this logarithmic plot: the number of missing values is about an order of magnitude larger when LOCAL MODE acquisitions are taking place.

A close inspection of the data quality in these files also revealed that missing values are often associated with "poor" or "fair" radiance values (with an RDQI value of 2 or 1, respectively) in their immediate vicinity. Figure 4 shows the time series of all poor values found in the four spectral bands and nine cameras for BLOCK 110 of all available ORBITs of PATH 168 between the start of the mission and 23 Decem-
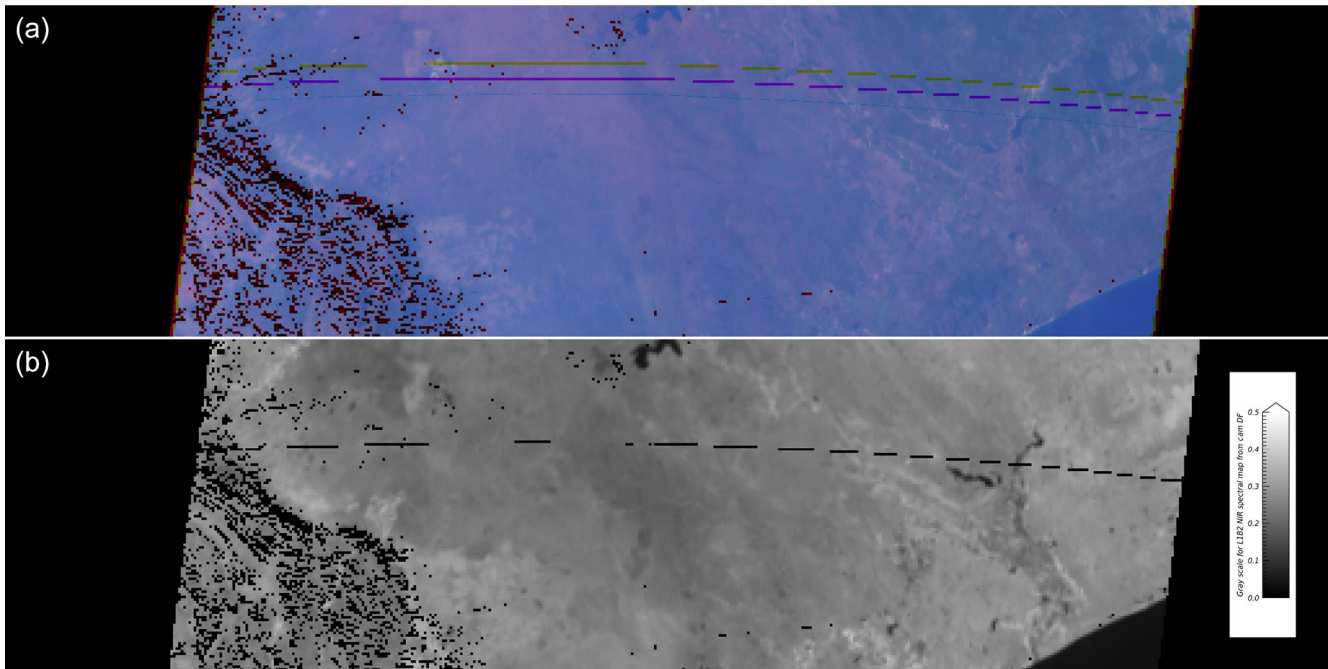
Figure 2. (a) Example of the effect of missing lines in a multispectral product, here an RGB composite of the red, green and blue spectral bands for the L1B2 terrain-projected GLOBAL MODE Brf data for the same DF camera case exhibited in Fig. 1. The top (yellow), middle (magenta) and bottom (light cyan, barely visible because of the general bluish tone of the image) lines correspond to the missing data in the blue, green and red spectral bands, respectively. This image was generated by first replicating the low-resolution blue and green pixels so as to match the resolution of the red band and then creating the composite image at the full spatial resolution. **(b)** Map of the NIR Brf of the same DF camera. The linear dimensions are the same as in Fig. 1. The three RGB spectral channels are stretched from 0.0 to 0.35 for the purpose of generating the color image, while the NIR data are stretched between 0.0 and 0.5.
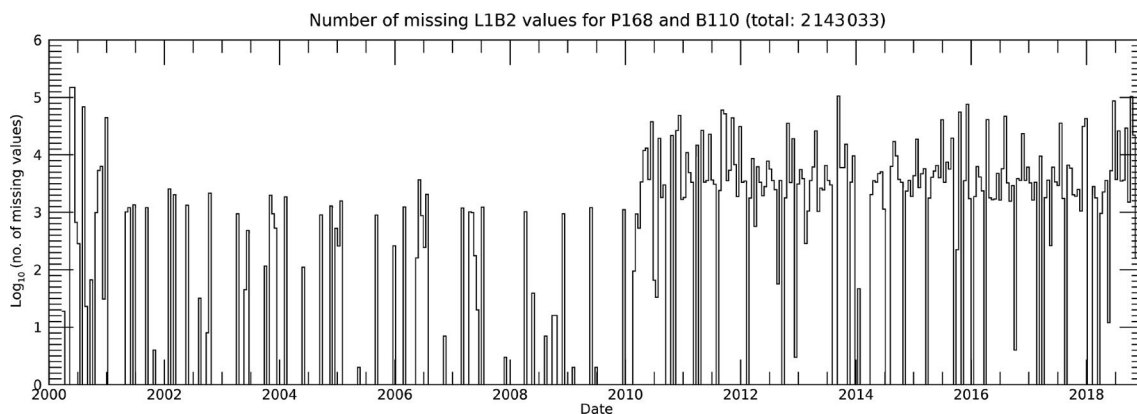
Figure 3. Time series of the logarithm in base 10 of the number of missing pixel values in the four spectral bands of the nine cameras of BLOCK 110 from each available MISR L1B2 GRP ORBIT in PATH 168 between March 2000 and December 2018. This BLOCK includes the Skukuza flux tower located in Kruger National Park in South Africa. LOCAL MODE data were briefly acquired at the start of the mission to support the Safari-2000 campaign and then systematically from December 2009 onward. It can be seen that there is a strong relationship between the number of missing values and the acquisition of LOCAL MODE data, although the latter is not the only process responsible for missing data.

ber 2018. Some 918 420 values fell into that category during that period: that brings the total number of missing or poor values to over 3 million for that particular PATH and BLOCK.

These findings call for multiple comments:

– While these numbers appear large (out of context), they remain tiny compared to the total number of "good" and "fair" pixel values (i.e., those associated with an RDQI of 0 or 1), which is of the order of 25×10^9 pixels for the
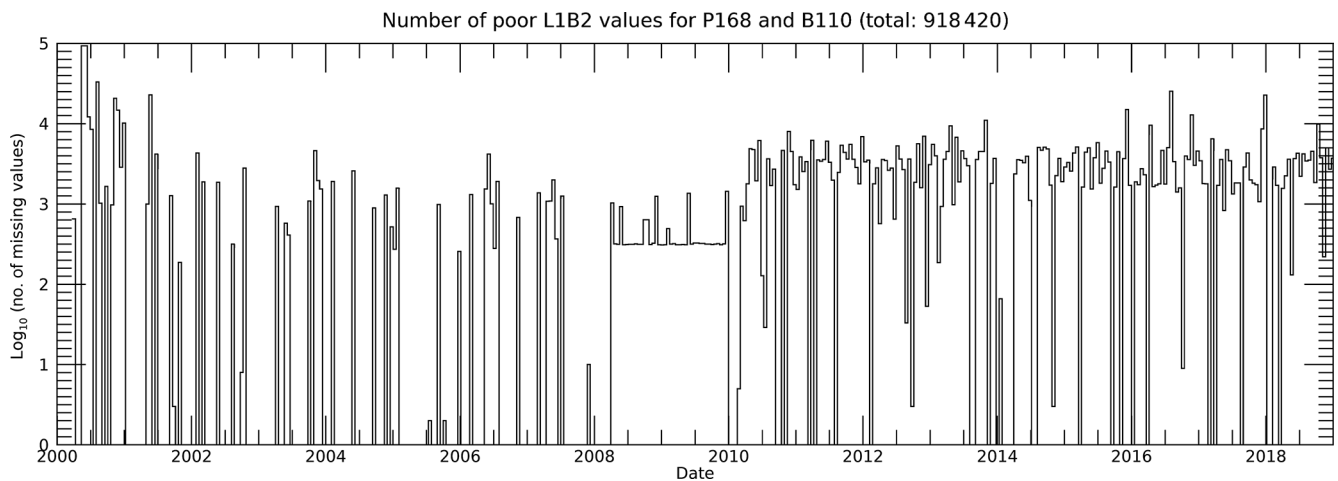
Figure 4. Time series of the logarithm in base 10 of the number of poor pixel values, in this case in the four spectral bands of the nine cameras of BLOCK 110 from each available MISR L1B2 GRP ORBIT in PATH 168 between late March 2000 and December 2018 (the same BLOCK as in Fig. 3). See the text for a discussion of the similarities and differences between those two time series.

same BLOCK and time period. So this problem does not affect the usability of the MISR instrument, especially for studies involving large areas or long periods of time.

– However, for the technical reasons described above, missing values are often concentrated in geographical areas where LOCAL MODE acquisitions take place. Hence, if a site is systematically acquired in LOCAL MODE over a substantial period of time, then that region tends to be more affected by this problem than other areas. This, in turn, implies that local studies, field campaigns or projects that occur precisely in those areas and time periods may be severely impacted, while similar investigations elsewhere may be relatively unaffected.

– There are somewhat fewer poor values than missing values in general, but there is also less difference in the peak number of poor values with or without LOCAL MODE acquisitions. This is because measurements affected by sun glint are typically marked as poor. This natural phenomenon occurs systematically and may affect a camera irrespective of whether LOCAL or GLOBAL MODE is used for acquisition, especially whenever the observed scene contains substantial water bodies.

– Nevertheless, as was the case for L1B2 radiance values, the number of poor values also increased by about an order of magnitude whenever the Skukuza site was systematically observed in LOCAL MODE.

– Figure 4 also reveals that a significant number of radiance measurements were assigned an RDQI of 2 between about March 2008 and the end of 2009 for reasons that remain to be investigated but that probably in-

volve changes in the software processing system rather than the performance of the instrument.

CE2: Unfortunate…

The study of Mahlangu et al. (2018) provides a good example of the crippling effect of these missing and poor data on a particular investigation: an airborne lidar CE2 field campaign took place in and around the Skukuza site in April 2012. The aim of that study was (1) to document the structure of vegetation using the lidar as high-spatial-resolution reference data over a limited area and (2) to explore whether a relationship between these airborne measurements and MISR-derived products could help describe those ecosystem properties over a larger region. It relied on products to characterize the plant canopy generated by the MISR-HR processing system (Verstraete et al., 2012, Version 1.04-5) for the closest available acquisition, namely PATH 168, ORBIT 65487 and BLOCK 110, acquired on 10 April 2012. The MISR-HR processing system is a set of algorithms designed to regenerate best estimates of the MISR data at the full spatial resolution in all 36 data channels. Figure 5 demonstrates the problem: the spatial coverage of the leaf area index (LAI) product over the BLOCK was significantly reduced by clouds (screened out on square areas of 17.6 km by 17.6 km by the software and data available at the time that paper was generated), and the remaining clear area was very much contaminated by missing data lines in all four spectral bands of two different cameras (AF and CA).

In summary, MISR L1B2 data loss can occasionally occur anywhere and at any time and will involve tens of thousands of missing values over a period of 10 years. However, in the neighborhood of a site that is systematically monitored in LOCAL MODE, the data loss can amount to multiple millions of missing values over the same period. These losses will be of little consequence for climatological studies, but they may cripple local applications.
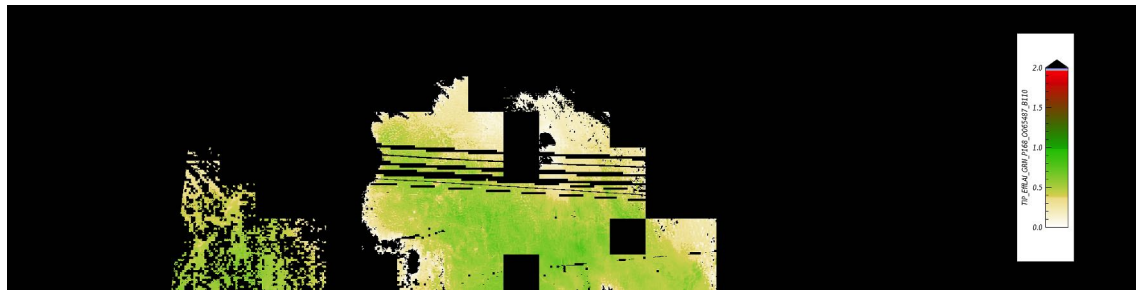
Figure 5. Example of the effect of missing lines in a derived product, here the leaf area index (LAI) for the particular date and time when an airborne field campaign was taking place in Kruger National Park in South Africa (the same PATH 168, ORBIT 65 487 and BLOCK 110 as for Figs. 1 and 2; see text for details). A large fraction of the MISR BLOCK is unavailable (depicted in black) due to the prevailing cloud cover on that particular date as well as the presence of missing lines. The color gradient (white, yellow, green, red) maps the LAI range [0.0, 2.0].

To address this issue and avoid serious contamination of subsequent analyses and products generated by the MISR-HR processing system (Verstraete et al., 2012), the radiance values that are missing and, optionally, those associated with an RDQI of 2 should be replaced by best estimates of what the original measurements would likely have been. The next sections describe the proposed solution to this problem, exhibit some results and document the performance of the algorithm.

3 Materials and methods

3.1 MISR data

The MISR mission is run by a group of engineers and scientists at NASA's Jet Propulsion Laboratory (JPL) in Pasadena, California, supported by an international team of researchers, while the data generated by this instrument and the standard products derived from the raw measurements are processed and permanently archived at NASA's Atmospheric Science Data Center (ASDC) in Hampton, Virginia. As is the case for other Earth observation missions, all MISR data products are freely available to anyone interested, either through customized orders or through bulk downloads from the data pool at https://eosweb.larc.nasa.gov/project/misr/misr_table (last access: 29 May 2020).

Three standard data sets are of direct relevance for the current purpose: the Ancillary Geographic Product (AGP) and two out of the six parameter sets of the Level 1B2 Georectified Radiance Product (GRP). These are the terrain-projected top-of-atmosphere (ToA) radiance GLOBAL MODE parameter and the Radiometric Camera-by-camera Cloud Mask (RCCM; Bull et al., 2011, p. 56).

3.1.1 The AGP data set

The AGP is the master reference data set containing essential information on the latitude and longitude of BLOCK locations as well as ancillary data such as the expected distribution of land masses and water bodies (in particular oceans; Bull et al., 2011, p. 14). This primitive land cover map actually recognizes seven different types of "surface features" (Bull et al., 2011, p. 210):

– 0: shallow ocean

– 1: land

– 2: coastline

– 3: shallow inland water

– 4: ephemeral water

– 5: deep inland water

– 6: deep ocean.

The spatial distribution of these feature types is fixed throughout the mission: it is not intended as a genuine, detailed land cover map but as a coarse land–sea partition with a few more features. In the current context, categories 0, 5 and 6 are merged into a water class, and the remaining categories are assigned to the land class. The results described in this paper are based on the AGP version `F01_24`.

3.1.2 The terrain-projected ToA radiance Global Mode parameter set

This parameter set is the primary MISR radiance product at the nominal top of the atmosphere (ToA): all higher level products, including the RCCM described in the next subsection, are derived from an analysis of those calibrated and geolocated measurements. In the default GLOBAL MODE, two versions of that parameter set are generated: one in which all measurements are projected on the World Geodetic System 1984 (WGS 84) reference ellipsoid (primarily used in applications over oceans) and one where measurements are projected on a digital elevation model (DEM; primarily used over land). This paper is concerned exclusively with this latter projection. All results described in this paper are based

Table 2. Correlation statistics between the radiance in the four spectral bands of the target (Tgt.) camera DF and the radiance in the best-correlated source (Src.) data channels (first attempt) using all common and valid values for the GLOBAL MODE measurements acquired in PATH 168, ORBIT 68 050 and BLOCK 110. The columns entitled "No. pix.", "RMSD", "PCC" and "χ^2" provide the number of valid measurements common to both data channels, the root mean square difference between the data channel values, the Pearson correlation coefficient between them and the value of the statistics for the linear fit between those data channels, respectively.

Tgt. cam.	Tgt. band	Src. cam.	Src. band	No. pix.	RMSD	PCC	χ^2
DF	Blue	CF	Blue	45 779	16.32	0.951	71 875
DF	Green	CF	Green	45 941	5.283	0.969	53 560
DF	Red	CF	Red	76 2392	2.409	0.977	2 230 000
DF	NIR	CF	NIR	46 186	1.741	0.989	129 323

on the L1B2 terrain-projected Georectified Radiance Product version `F03_0024`.

3.1.3 The RCCM parameter set

The Radiometric Camera-by-camera Cloud Mask (RCCM) provides a separate cloud mask for each of the nine MISR cameras. This standard data set is described in detail in the Level 1 cloud detection Algorithm Theoretical Basis Document (ATBD; Diner et al., 1999b), which can be downloaded from https://eospso.gsfc.nasa.gov/atbd-category/45(last access: 29 May 2020), and in subsequent papers such as Zhao and Di Girolamo (2004) and Yang et al. (2007). All results described in this paper are based on the RCCM version `F04_0025`.

Over land, these camera-specific cloud masks are derived from the L1B2 radiance data described in the previous subsection using the red and the near-infrared (NIR) spectral bands of each camera. Hence, whenever there are missing data in those spectral bands, there will be missing data in the RCCM product too. However, a procedure to replace missing data in those cloud masks has recently been designed and is fully documented in Verstraete et al. (2020).

3.2 Correlation between the target and the sources

A practical solution to the problem described in Sect. 2 above (i.e., restoring data when there are missing lines) is made possible by two findings: (1) as shown earlier, the missing pixels appear in different locations in different spectral channels of the affected camera, and (2) in most cases, it is possible to find for each data channel affected by missing or poor data one or more data channels (among the other 35 simultaneously acquired, i.e., for the same MISR PATH, ORBIT and BLOCK) that exhibit a very high correlation with the one in need of an update. In the rest of this paper, the data channel that is being repaired is called the *target*, and the other 35 data channels of the same data acquisition are called the *sources* (or predictors).

The Pearson correlation coefficients (CCs) between all pixel values that are valid (i.e., excluding all values with an RDQI value of 2 or 3) and common between the target and

each of the 35 source data channels are computed. In each of these 35 cases, the root mean square difference (RMSD) between the data channel values, the best linear fit between the source and the target, and the χ^2 value, i.e., a measure of the dispersion of the data points around that linear fit function, are also calculated. This set of statistics is then ranked in decreasing order of correlation coefficient value. It turns out that one or more source data channels are usually highly correlated (CC larger than 0.9) with the target data channel, thereby providing reliable means to replace the missing values in the target on the basis of nonmissing values in the most promising source data channel.

This approach is first demonstrated with the MISR GRP GLOBAL MODE data for PATH 168, ORBIT 68050, BLOCK 110 and camera DF exhibited in Fig. 2. Table 2 shows the statistics describing the relationships between the four target spectral bands of the DF camera and the best (i.e., the most promising in terms of the Pearson CC) identified sources (in this case the same spectral channels as the CF camera) using all valid pixels that are common to both data channels. The χ^2 value for the red band (or indeed for any high-resolution data channel) is much larger than for the other GLOBAL MODE data channels because they contain about 16 times more data points.

Figure 6 shows the scatterplots and the linear fits between the four target spectral bands of the DF camera case mentioned in Table 2 and the best predictor source data channels for the selected BLOCK.

While the correlations are highly significant, in part due to the large number of pixel values, the shape and the dispersion of the cloud of data points often suggest that a single linear equation may not always be optimal to predict the target values across the entire BLOCK. This is largely due to the fact that the scene may include rather different geophysical media, which are possibly governed by different statistical relationships as far as the correlations between data channels are concerned.

To explore this avenue, the sets of points used in these computations were partitioned into three categories: clear land masses, clear water bodies and cloud fields. For the specified PATH and BLOCK, the geographical distribution of
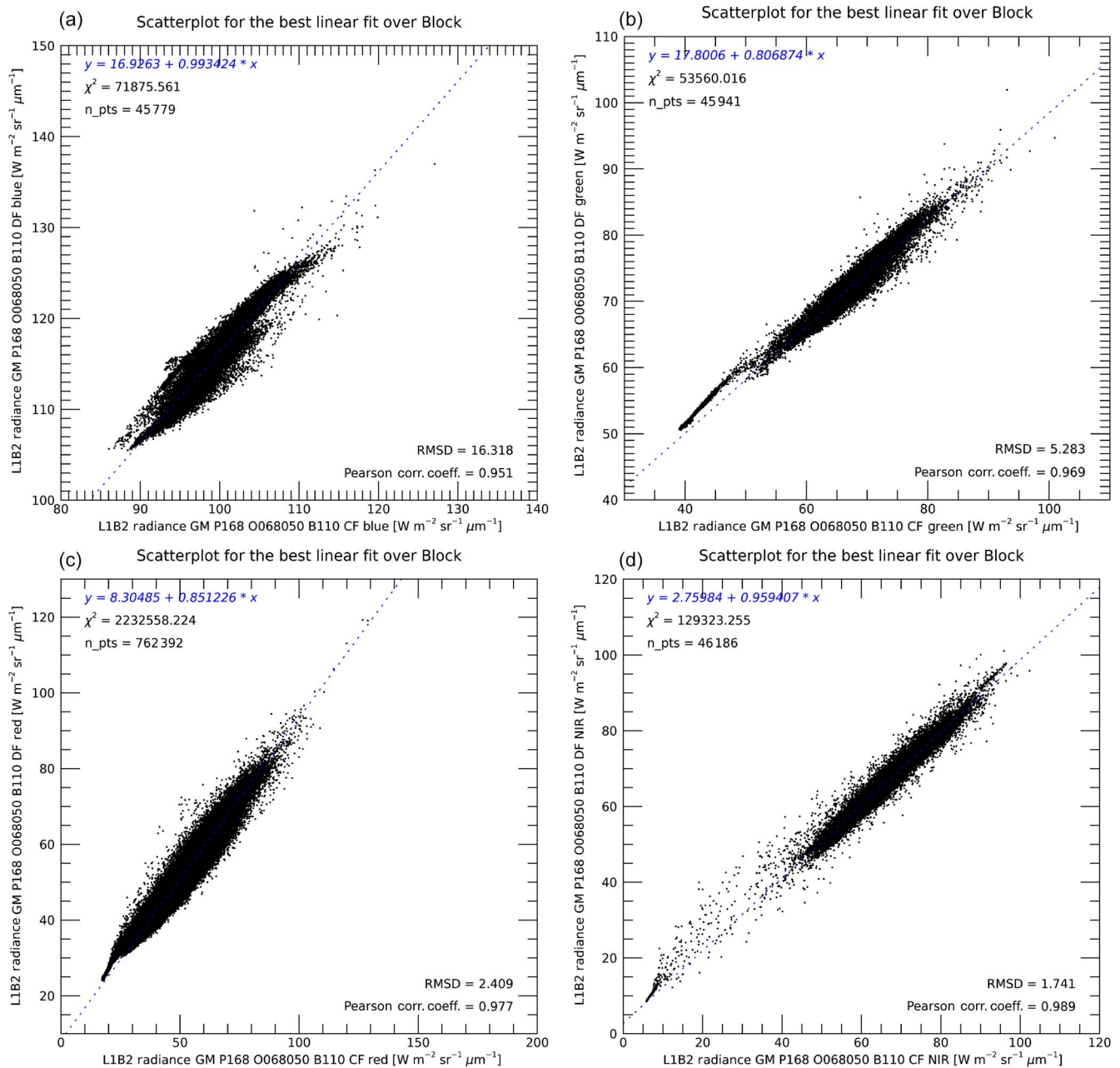
Figure 6. Scatterplots and best linear fit relationships to predict the radiance values of the four spectral bands of the target DF camera for the GLOBAL MODE measurements of PATH 168, ORBIT 68 050 and BLOCK 110 using all common valid values. In this case, the best predictors for the measurements by the DF camera were those acquired by the CF camera in the same spectral bands as the targets (**a**: blue; **b**: green; **c**: red; and **d**: NIR). Note that the ranges of values are different for each plot in order to optimize the view of the data.

land masses and water bodies was extracted from the MISR surface cover type map contained in the static AGP file described earlier. The cloud information was retrieved from the Radiometric Camera-by-camera Cloud Mask (RCCM) data product, updated as explained in Verstraete et al. (2020). Statistics, including the Pearson correlation coefficients and the best linear fit equations, were generated for each of these three categories. The gain in pursuing this approach is demonstrated in Fig. 7, which compares the best fit statistics while processing the NIR spectral band of camera AA for the same scene as above when all valid values available in the BLOCK are used for establishing the statistics (left panel) and when only those values attributable to clear land masses are used (right panel). The RMSD, the CC and the χ^2 statistics are significantly improved by focusing on the clear land masses only.
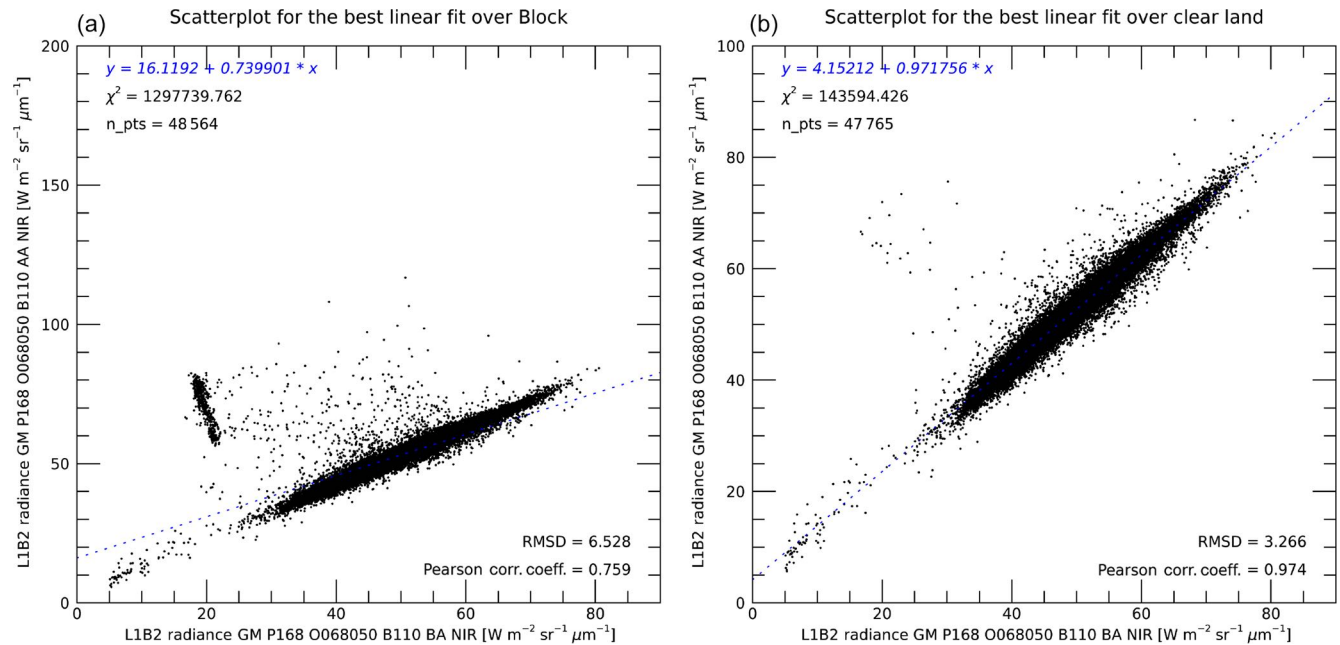
Figure 7. Scatterplots and best linear fit relationships to predict the radiance values of missing data in the NIR spectral band of the AA camera for the same GLOBAL MODE measurements of PATH 168, ORBIT 68 050 and BLOCK 110 as in Fig. 6. Panel **(a)** shows the results obtained when all common valid values throughout the BLOCK are considered, while panel **(b)** shows the statistical results applicable only to the clear land masses. The Pearson correlation coefficient, the RMSD and the χ^2 statistics are definitely improved in this latter case as a group of more than 800 pixel values, identified as clouds, is treated separately.

Table 3. Correlation statistics between the four spectral bands of the target camera DF and the best-correlated source data channels (first attempt) using all common and valid clear land values for the GLOBAL MODE measurements acquired in PATH 168, ORBIT 68 050 and BLOCK 110. The column headers are identical to those in Table 2.

Tgt. cam.	Tgt. band	Src. cam.	Src. band	No. pix.	RMSD	PCC	χ^2
DF	Blue	CF	Blue	44 729	16.27	0.957	63 244
DF	Green	CF	Green	44 866	5.132	0.962	49 093
DF	Red	CF	Red	744 596	2.242	0.974	2 150 000
DF	NIR	CF	NIR	45 066	1.652	0.982	120 534

Table 3 shows the statistical results for the same cases as before (Table 2), this time reporting values for clear land masses only. While the correlation coefficients are roughly equivalent despite the somewhat smaller number of points involved, the dispersion statistics (RMSD and χ^2) are again improved. Figure 8 exhibits the corresponding scatterplots and the best linear fit functions for clear land masses: as expected, these compare favorably to the results shown in Fig. 6 since this particular BLOCK is essentially cloud-free.

3.3   Replacement algorithm

These findings suggest that missing and, optionally, poor L1B2 radiance values could be replaced by reconstructed estimates based on the actual measurements obtained quasi-simultaneously in other data channels (spectral bands or cameras) for the same geographical location. This section out-lines the sequence of steps undertaken to achieve this goal in a schematic manner intended to also serve as a guide to the IDL[1] function `fix_l1b2.pro`, which implements these concepts in the open-source IDL processing software version 2.2.0 available from GitHub.

This function takes as input arguments pointers to the scaled radiances (with the RDQI attached), the unscaled radiances, the Brf and the RDQI data buffers for the specified MISR LOCAL or GLOBAL MODE, PATH, ORBIT and BLOCK, which must have been loaded on the heap prior to the call. This ensures fast access to those data fields as they will need to be read multiple times during the processing. An initial suite of preliminary steps are then undertaken to set the stage:

---

[1]IDL is a trademark of Harris Geospatial Solutions, Inc.
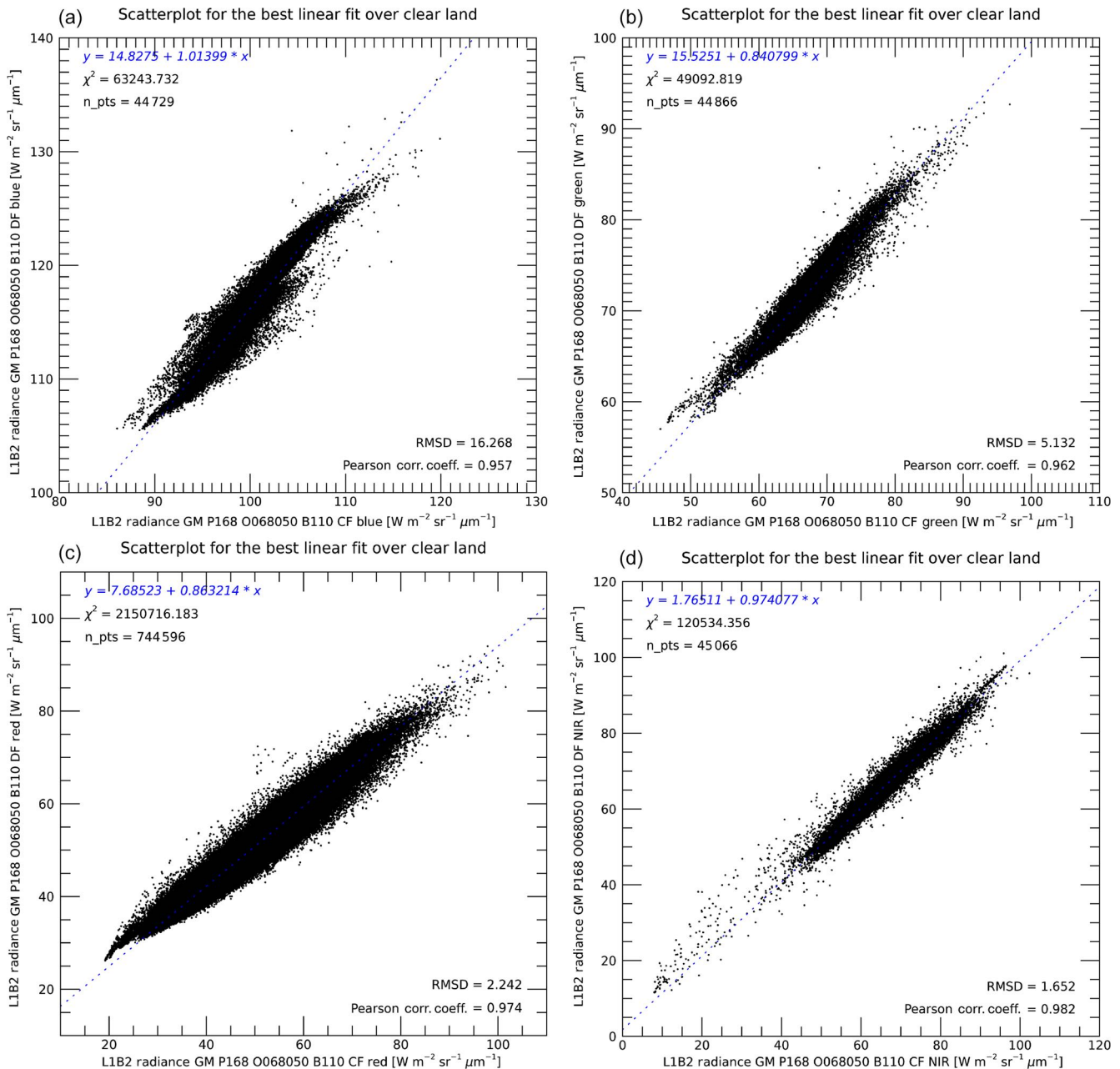
Figure 8. Scatterplots and best linear fit relationships to predict the clear land surface values of the four spectral bands of the DF camera for the GLOBAL MODE measurements of PATH 168, ORBIT 68 050 and BLOCK 110. In this case, the best predictors for the measurements by the DF camera were those acquired by the CF camera (**a**: blue; **b**: green; **c**: red; and **d**: NIR). Note that the ranges of values are different for each plot in order to optimize the view of the data.

- The IDL function offers the option of mapping the L1B2 product before processing to be able to show how the results of the processing differ from the original MISR data.

- The next step consists of generating the masks for clear land masses, clear water bodies and cloud fields to partition all valid radiance values found in the BLOCK into those three categories. Although statistics are in fact computed for clear water bodies and cloud fields, they are not reported here as the land areas are of primary interest.

- An optional main log file may be created to keep track of the progress and provide information on intermediary results, for instance for diagnostic purposes.

– The function `pre_fix_l1b2.pro` is then called to locate the numbers and positions of the poor and missing data values within each of the 36 data channels. If any are found, the function `best_fits_l1b2.pro` is activated to compute the optimal statistics and the best linear fit functions to replace those poor or missing values and to optionally generate a separate log file for each case. Information on progress is also added to the main log file if it has been requested in the previous step.

At that point, the code relies on two closely related functions, `fix_poor_l1b2.pro` and `fix_miss_l1b2.pro`, to replace poor (if required) and missing L1B2 values, respectively. The core of the processing is outlined in the following pseudocode listing[TS1]:   TS1: Yes, Appendix is a nicer solution.

```
FOR each camera
   FOR each spectral band
      access the MISR L1B2 data for the
      target
      retrieve the number and location
      of poor or missing values
      skip to the next camera/band
      combination if no values need
      replacement
      WHILE the maximum number of
      attempts has not been reached
         IF poor or missing values
         remain in the land/water/
         cloud target
            record the current best
            source and correlation
            statistics
            access the MISR L1B2 data
            for the current source
            upscale or downscale the
            source data to match the
            target resolution
            FOR each target value that
            needs replacement
               record the radiance
               value at the same
               location in the
               current source ensure
               that this source
               value is valid (i.e.,
               not missing or poor
               itself) apply the best
               linear fit equation for
               this attempt replace
               the poor or missing value
               in the target by this new
               estimate update the RDQI
               for that new value to 1B
            ENDFOR
```

```
            update the number and
            location of remaining
            missing (or poor) values
         ENDIF
         point to the next best source
         and correlation statistics
      ENDWHILE
   ENDFOR
ENDFOR
```

If poor values are replaced, the function `fix_poor_l1b2.pro` also optionally generates statistics and scatterplots of the updated versus the original values.

The `WHILE` loop over `attempts` is required because in some cases the best source data channel to replace values in the target data channel happens to also have missing values in the very same location as the target. In those cases, the next best data channel must be considered. The maximum number of attempts (i.e., the maximum number of best source data channels to consider) is specified as an argument to the function. Practical experience and considerations indicate that this value should generally be set to no more than 4: smaller values may result in nontrivial numbers of missing or poor values not being replaced, while larger values may result in the use of source data channels that are not as well correlated to the target and therefore result in less reliable replacement values being proposed. However, see Sect. 4.3 below for an exceptional case that required eight iterations to replace most missing values. Note also that replaced values are always assigned an RDQI of 1.

4 Results

The following exhibits will graphically show the outcome of this process for the cases discussed in Sect. 2 above.

4.1 Global Mode, Path 168, Orbit 68050, Block 110, camera DF

The particular case exhibited earlier in Fig. 2, where four spectral bands of the DF camera exhibit missing and poor data values, is examined first.

Figure 9 shows the outcome of the process where the missing values in the original target data channels are replaced by the values estimated from the source data channels indicated in Table 3 for the very same geographical location and inserted into the linear fit equations exhibited in Fig. 8. The top frame is an RGB composite, and the bottom frame shows the map of the corresponding NIR spectral band. These frames can be compared to those exhibited in Fig. 2.

4.2 Global Mode, Path 168, Orbit 65487, Block 110, camera CA

The case exhibited earlier in Fig. 5 is examined next. Table 4 summarizes the correlation statistics between the four spec-

Earth Syst. Sci. Data, 12, 1–25, 2020   https://doi.org/10.5194/essd-12-1-2020

Table 4. Correlation statistics between the four spectral bands of the target camera CA and the best-correlated source data channels using only common and valid clear land values for the GLOBAL MODE measurements acquired in PATH 168, ORBIT 65 487 and BLOCK 110. The column headers are identical to those in Table 2.

Tgt. cam.	Tgt. band	Src. cam.	Src. band	No. pix.	RMSD	PCC	χ^2
CA	Blue	CA	Green	17 591	22.48	0.966	156 441
CA	Green	CA	Blue	17 591	22.48	0.966	119 634
CA	Red	DA	Red	268 707	10.47	0.955	11 400 000
CA	NIR	DA	NIR	15 613	6.866	0.969	58 113
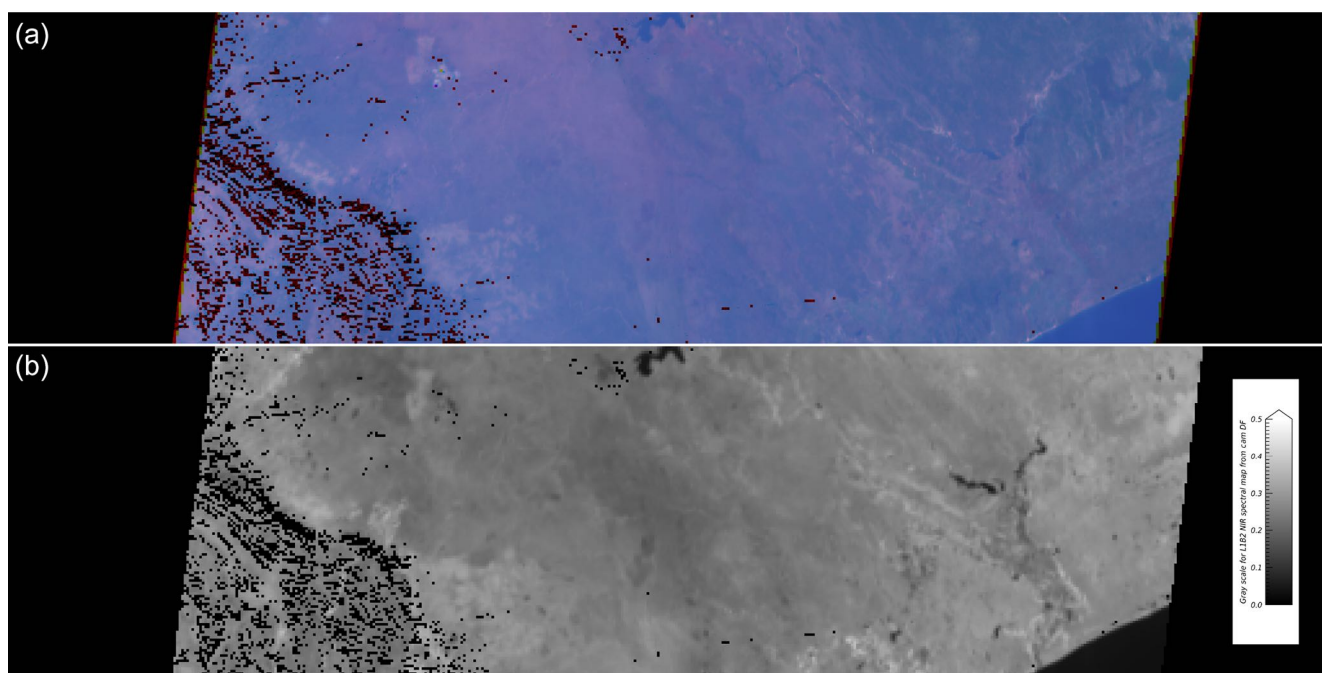
Figure 9. (a) RGB composite map of the red, green and blue spectral bands for the L1B2 terrain-projected GLOBAL MODE bidirectional reflectance factor data file for the same DF camera case exhibited in Fig. 2. **(b)** Map of the NIR spectral band for the same DF camera. All missing values in the original data files have been replaced by estimates as described in the text. The linear dimensions are the same as in Fig. 1, and all three visible spectral channels are stretched from 0.0 to 0.35 for the purpose of generating the color image; the gray scale used to stretch the NIR data for the bottom frame assigns black to reflectance values of 0.0 and white to values of 0.50 or higher.

tral bands of the CA camera, all affected by missing values, and the best sources to estimate replacement values considering only the valid values in clear land masses that are common to the target and the source data channels.

Figure 10 exhibits maps of the RDQI for those four data channels of the CA camera. The relative displacement of missing lines between the spectral bands and the clustering of poor values around those lines are clearly observable: these findings have been widely confirmed in all cases investigated.

Note that the best predictor for missing and poor values in the CA/blue data channel is the CA/green data channel and conversely. Since the RMSD and the Pearson correlation coefficient are symmetric with respect to their inputs, the statistics are identical in these cases. However, the CA/green data points fit a little bit better than the best linear function (the χ^2 for the function predicting CA/green is somewhat lower

than that for CA/blue). The best predictors for the CA/red and CA/NIR data channels are provided by the DA camera in the corresponding spectral bands.

The scatterplots for these four cases are exhibited in Fig. 11. It can be seen that the best fit function to predict the CA/red data channel is not as good as for the other data channels, although the Pearson correlation coefficient is still 0.836. These statistics are of course also affected by the fact that there are much fewer valid data values available to estimate the missing and poor pixels compared to the earlier case of ORBIT 68 050.

Using those best linear functions and the valid values in the source data channel, it is possible to generate estimates of the missing and poor values in the target data channel. Figures 12 and 13 exhibit the RGB composite map of the first three spectral bands and the B&W map of the NIR spectral
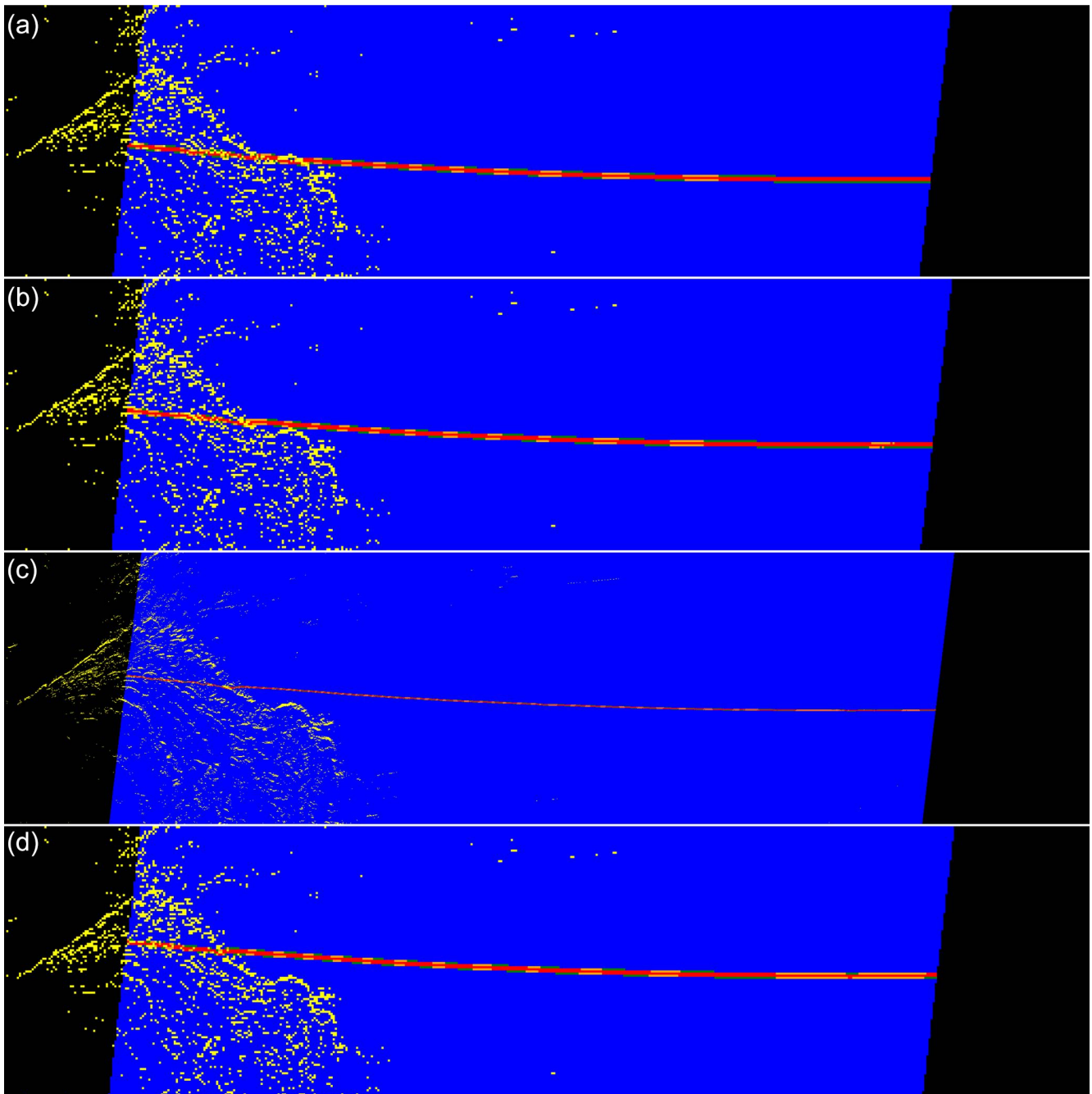
Figure 10. Spatial distribution of RDQI values for GLOBAL MODE, PATH 168, ORBIT 65 487, BLOCK 110 and camera CA in the four spectral bands (from top to bottom: blue, green, red and NIR). Black: edge pixels; yellow: pixels obscured by the local topography; blue: RDQI = 0; green: RDQI = 1; orange: RDQI = 2; red: RDQI = 3.
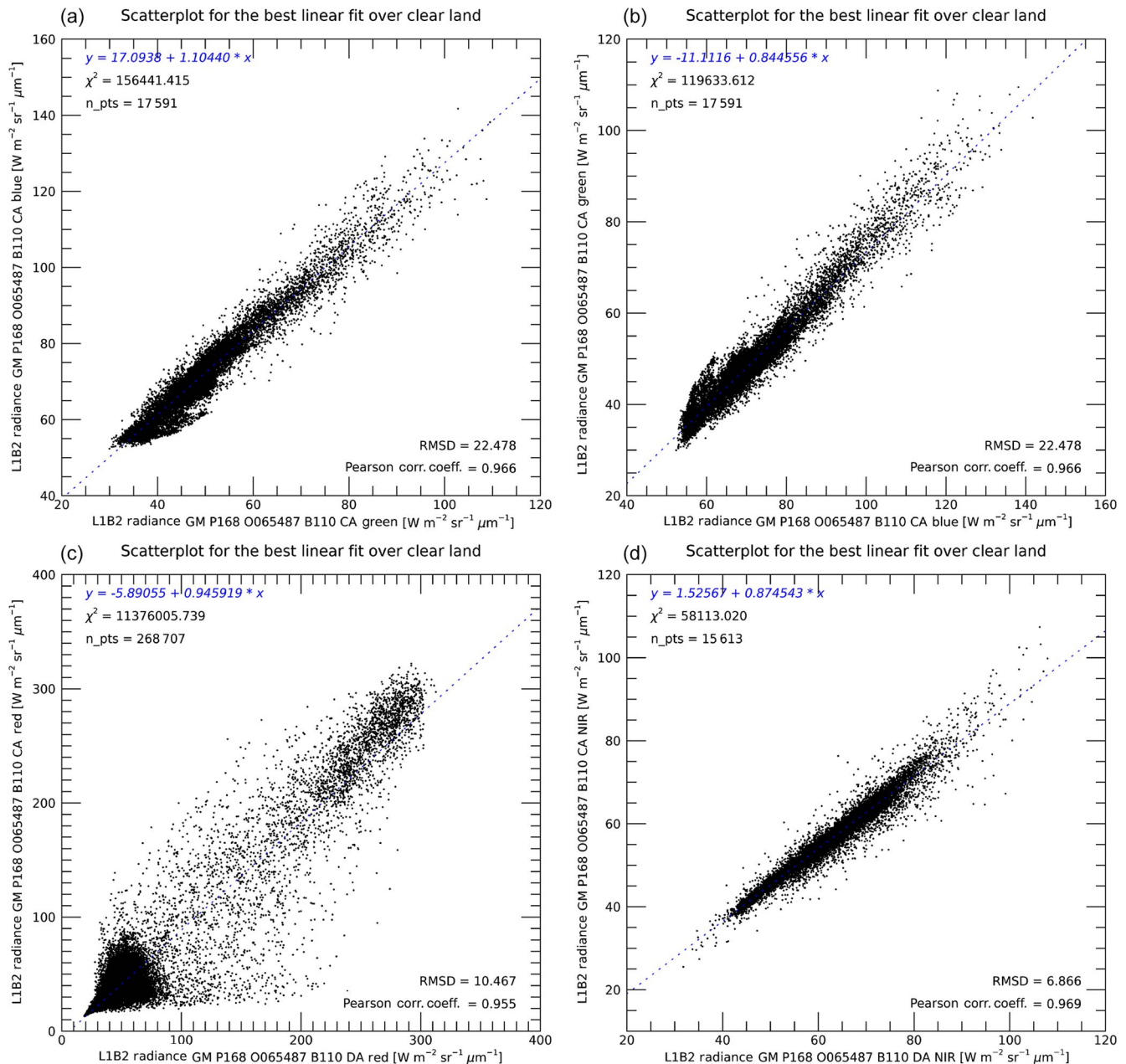
Figure 11. Scatterplots and best linear fit relationships to predict the values of the four spectral bands of the target CA camera for the GLOBAL MODE measurements of PATH 168, ORBIT 65 487 and BLOCK 110. **(a)** Blue, **(b)** green, **(c)** red and **(d)** NIR.

band of the CA camera before and after the replacement of missing values.

4.3 Global Mode, Path 168, Orbit 2111, Block 110, camera BA

The next instance exhibits the most severe case of missing values encountered so far in our investigations. Figure 14 shows the RDQI values for the four spectral bands of the BA camera for P168, O002111 and B110.

The original bidirectional reflectance factor products for these same four spectral bands are shown in Fig. 15: it can be seen that missing values severely affect the usability of the data acquired by this camera.

Figure 16 exhibits the updated bidirectional reflectance factor values in each of the four spectral channels after processing those data as described above (exceptionally allowing for eight successive attempts due to the significant overlap between the areas affected by missing values).
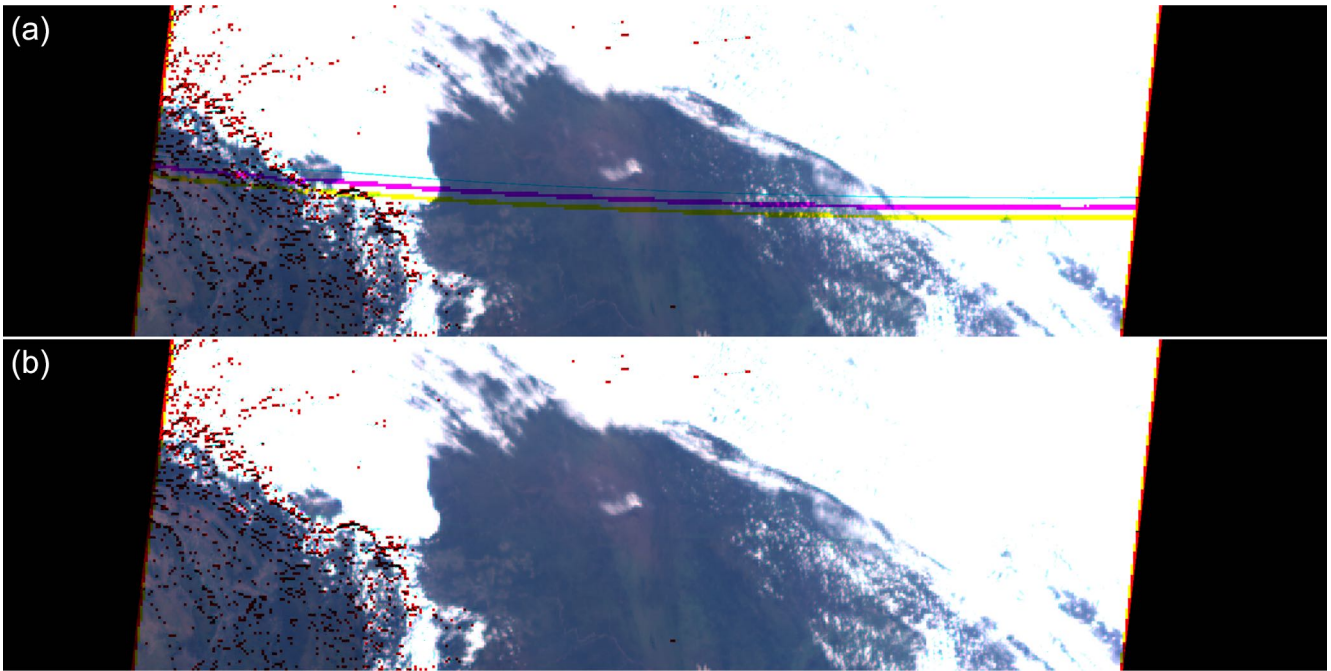
Figure 12. RGB maps of the three visible data channels for GM-P168-O065487-B110-CA **(a)** before and **(b)** after replacing the missing and poor data values with the best estimates computed as described above.
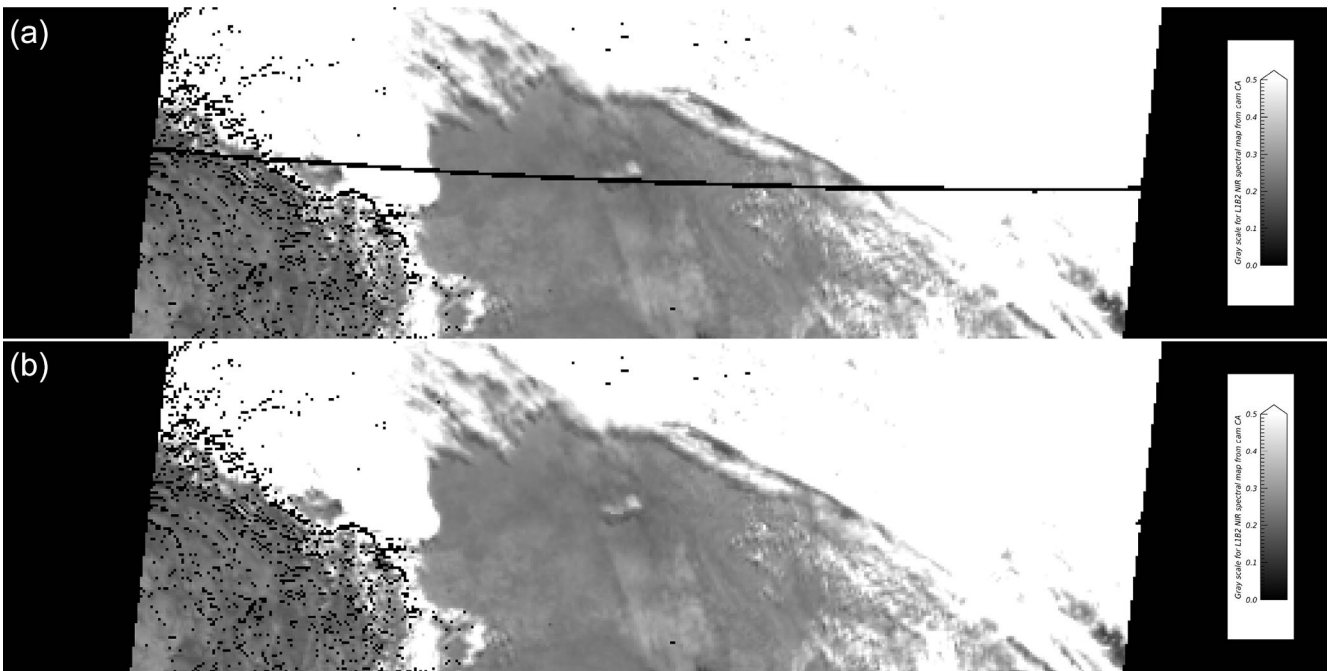
Figure 13. Maps of the GM-P168-O065487-B110-CA-NIR Brf data channel **(a)** before and **(b)** after replacing the missing and poor data values with the best estimates computed as described above.
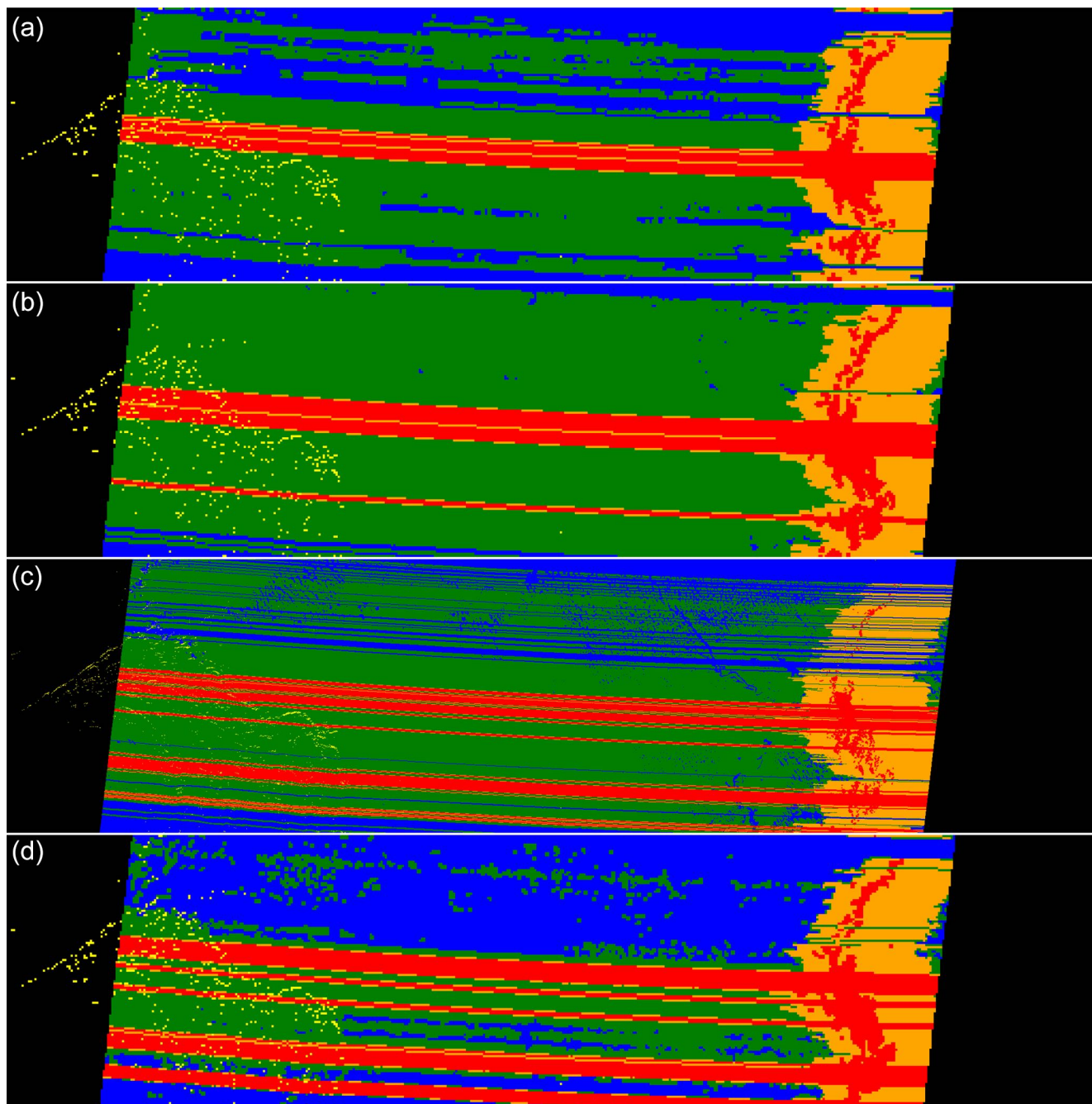
Figure 14. Maps of original RDQI values for GM, P168, O002111, B110 and camera BA in (from top to bottom) the blue, green, red and NIR spectral bands. The linear dimensions are the same as in Fig. 1, and color coding is as described in the legend of Fig. 10.

5   Algorithm evaluation

While the results exhibited in the previous section may be visually impressive, it remains essential to assess the numerical accuracy of this procedure. Since it is not possible to evaluate the pertinence of the replaced values when the original data are missing, the process will be appraised by artificially introducing missing values to files that do not have missing

lines in the first place and then comparing the reconstructed values against the original ones.

The original valid data are first recorded separately, and missing values are inserted in MISR GLOBAL MODE data files for PATH 168, ORBIT 68 050 and BLOCK 110 between lines 30 and 34 of the green spectral band in camera CF, lines 100 to 110 of the red spectral band in camera AN and lines 50 to 54 of the NIR spectral band in camera DA. Fig-
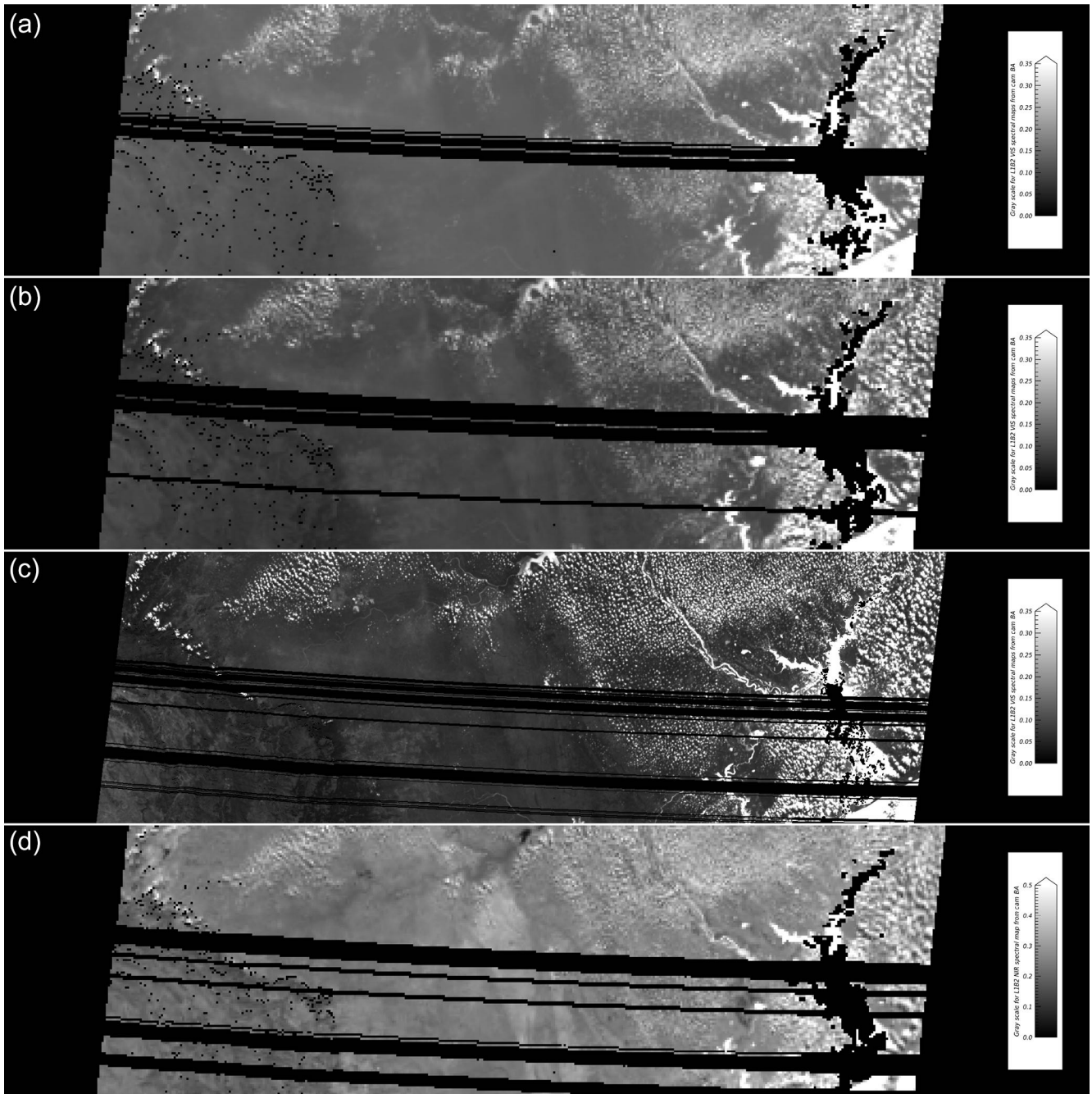
Figure 15. Maps of the original ToA bidirectional reflectance factor values for GM, P168, O002111, B110 and camera BA in (from top to bottom) the blue, green, red and NIR spectral bands. The linear dimensions are the same as in Fig. 1, and gray scale stretching is the same as before: it assigns black to a null reflectance and white to reflectances of 0.35 or more in the blue, green and red spectral bands and 0.50 in the near-infrared spectral band.

ure 17 shows the corresponding maps with missing black lines clearly visible. Note the difference between the artificially missing straight lines and the curved lines that occur when data are missing following an instrument issue as well as the rather larger areas affected.

These data files are then processed as before, and the three left panels of Fig. 18 exhibit the correlation statistics for the data channels that are best correlated with those that need to be updated. The three panels shown on the right compare the original values in abscissa to the reconstructed values in ordinates.
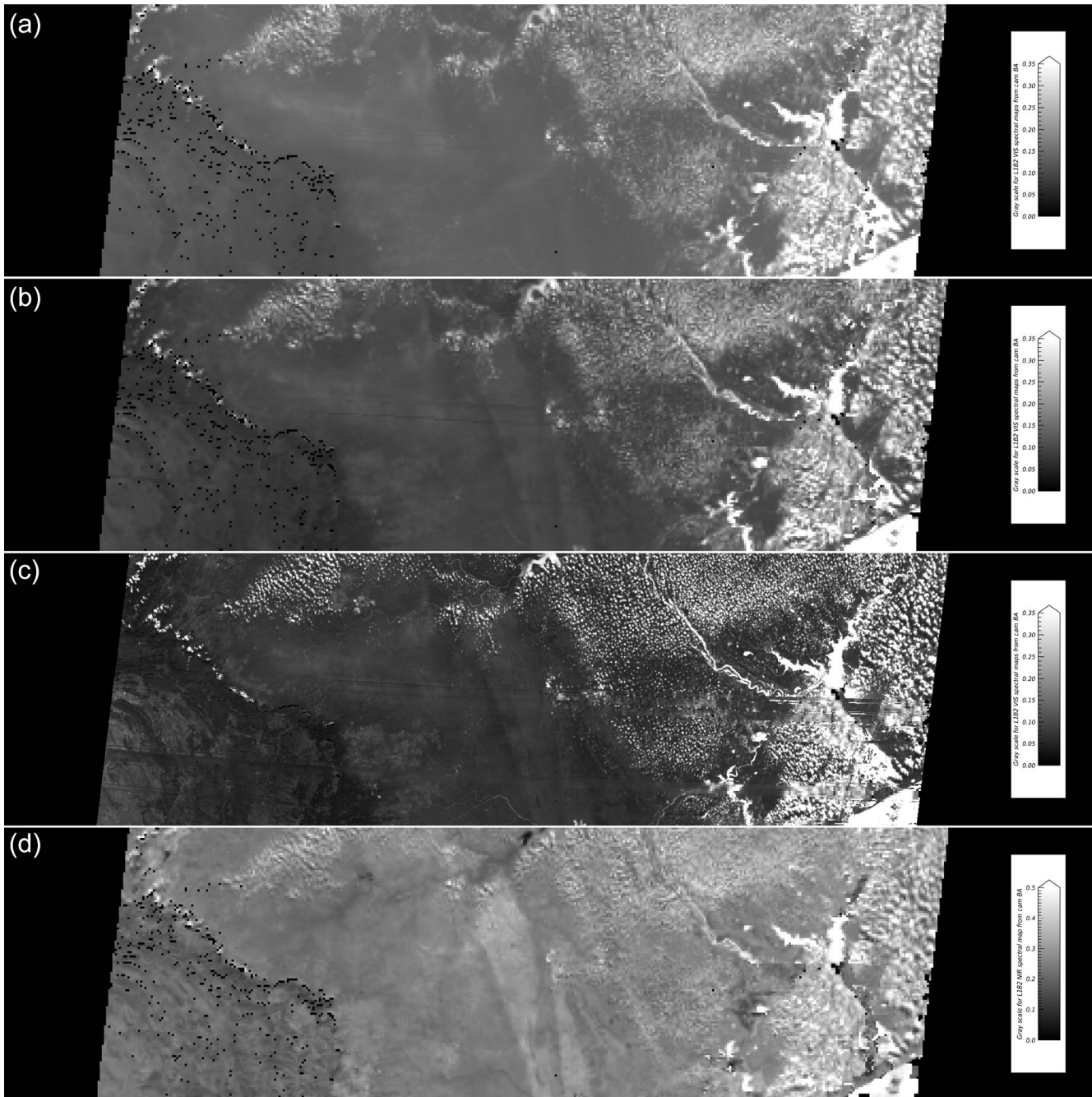
Figure 16. Maps of the updated ToA bidirectional reflectance factor values for GM, P168, O002111, B110 and camera BA in (from top to bottom) the blue, green, red and NIR spectral bands. Achieving this level of replacement required eight iterations (see text for details). The linear dimensions are the same as in Fig. 1, and gray scale stretching is the same as before: it assigns black to a null reflectance and white to reflectances of 0.35 or more in the blue, green and red spectral bands and 0.50 in the near-infrared spectral band.

Figure 19 exhibits the maps of those three data channels where the missing data have been replaced by best estimates obtained as described above.

Similar results have been obtained in all other cases inspected. A second example is considered next for the case of P168, O065487, B110 documented in Figs. 10, 11, 12 and 13, which includes significant cloud cover. In this case too, the original data channels CF/green, AN/red and DA/NIR do not suffer from any missing values so the same patterns of missing data as described above were artificially inserted in the original data, which were then processed as indicated above. Table 5 provides the number of missing points effectively
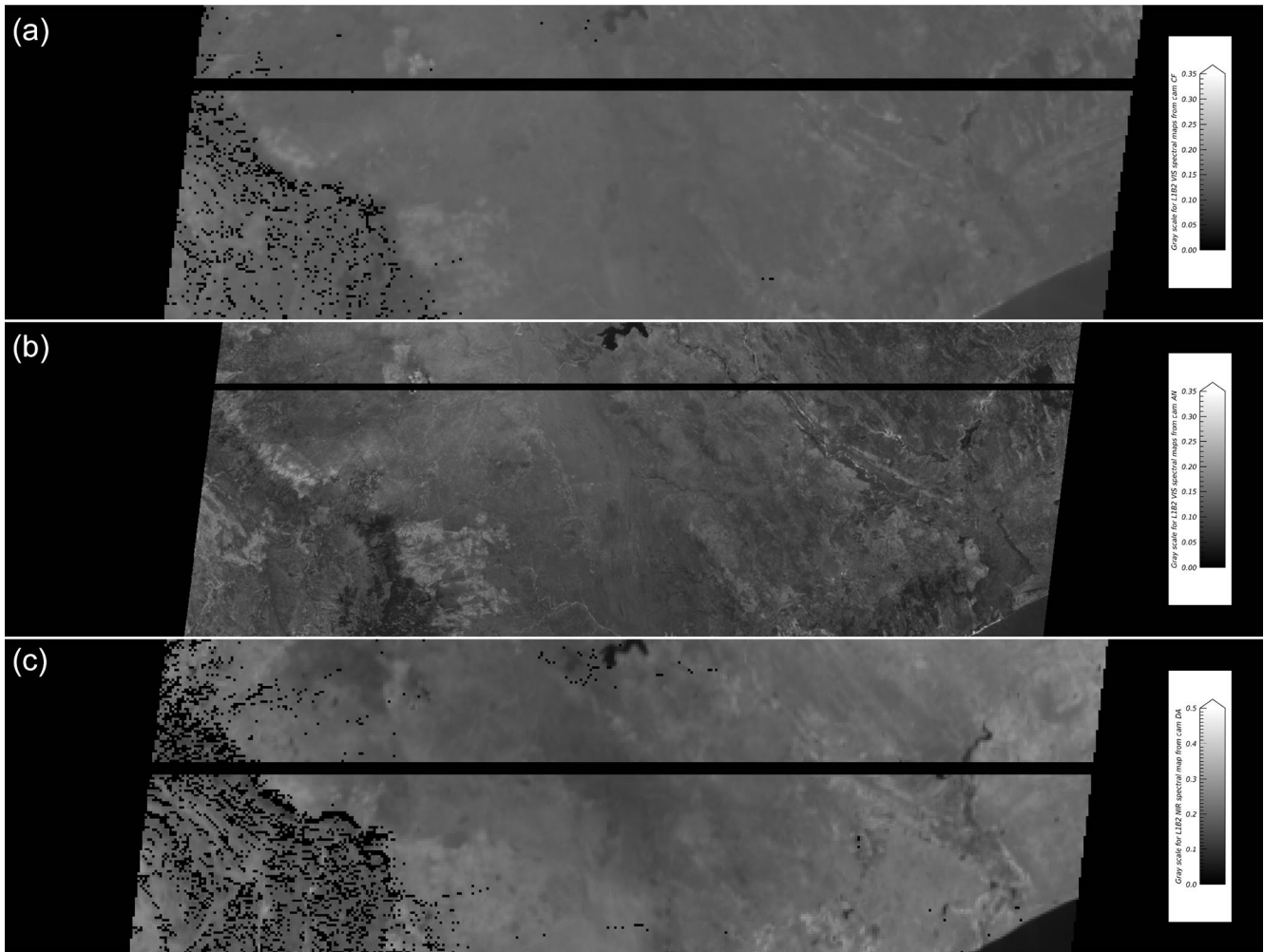
Figure 17. Maps of the MISR L1B2 data channels for the CF/green, AN/red and DA/NIR data channels of P168, O068050 and B110, where missing data have been inserted artificially for the purpose of testing the algorithm described in this paper. The linear dimensions are the same as in Fig. 1, and gray scale stretching is the same as before: it assigns black to a null reflectance and white to reflectances of 0.35 or more in the blue, green and red spectral bands and 0.50 in the near-infrared spectral band.

replaced over clear land masses, the root mean square difference and the Pearson correlation coefficient between the original and the reconstructed data as well as χ^2, the unreduced chi-square statistic that expresses the goodness of fit of the linear relationship between those two data sets. As noted before, the χ^2 statistics for the AN/red data channel are higher due to the much larger number of pixel values involved. Note also that the number of clear land values effectively replaced depends on the cloudiness present in the scene and therefore on the position of the artificially introduced lines of missing data within the BLOCK.

Table 5. Performance statistics showing the high correlation between the original and the reconstructed MISR L1B2 radiance data over clear land masses when missing data are artificially introduced to the original data files for GLOBAL MODE P168, O065487, B110. The numbers of clear land values involved depend on the cloudiness present in the scene and therefore on the position of the artificially introduced lines of missing data within the BLOCK.

Channel	No. of points	RMSD	PCC	χ^2
CF/green	165	3.915	0.990	574
AN/red	1136	2.415	0.990	2762
DA/NIR	600	2.632	0.930	3512
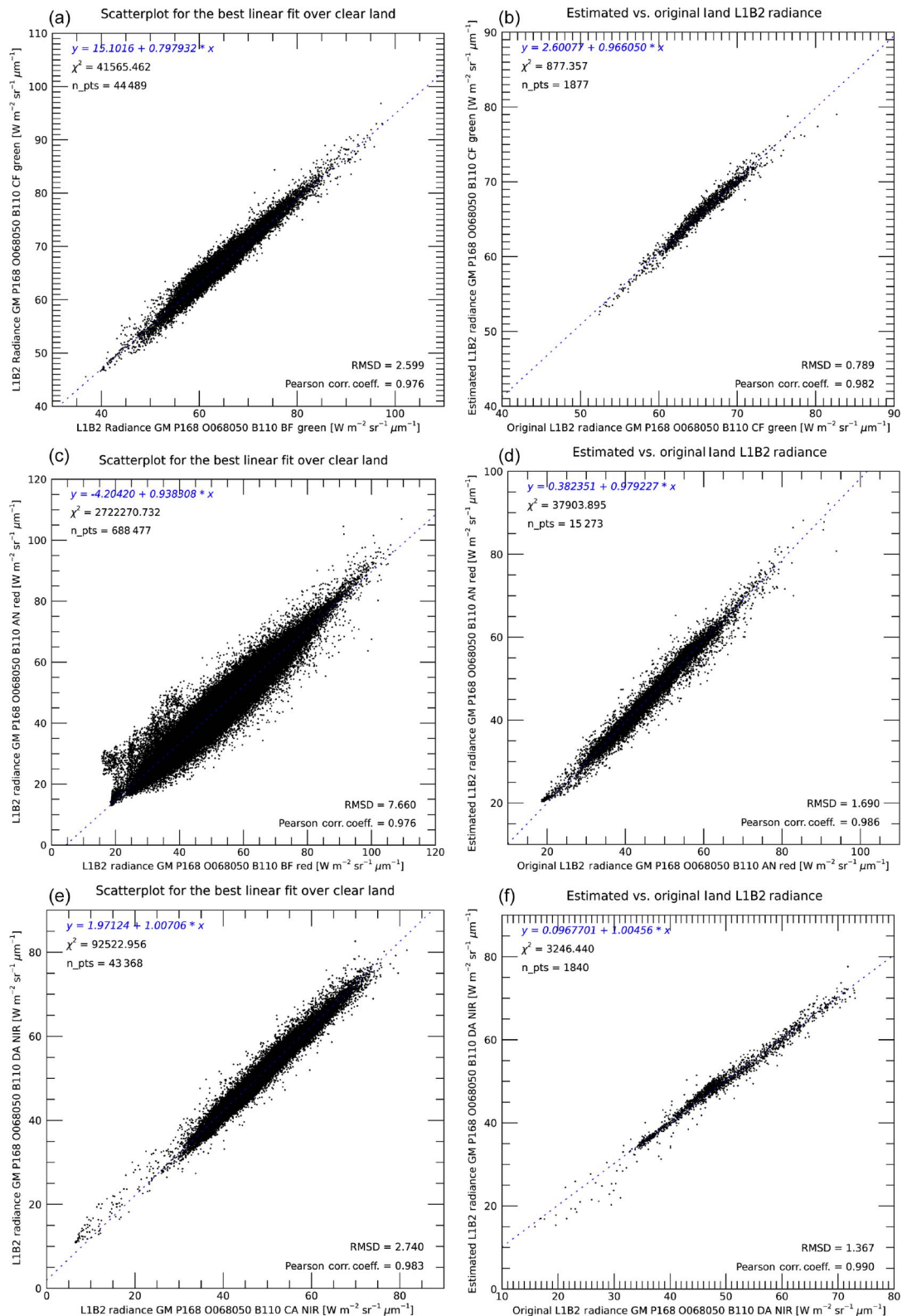
Figure 18. Scatterplots of the reconstructed versus the original values in the three data channels where missing values were artificially introduced as shown in Fig. 17: the top, middle and bottom panels concern the CF/green, AN/red and DA/NIR data channels, and in each case, the left panel shows the best predictor (abscissa) for the affected data channel (ordinate), while the right panel exhibits the relationship between the original (abscissa) and the reconstructed (ordinate) values in the areas where missing values were artificially introduced. Note that the ranges of values are different for each plot in order to optimize the view of the data.
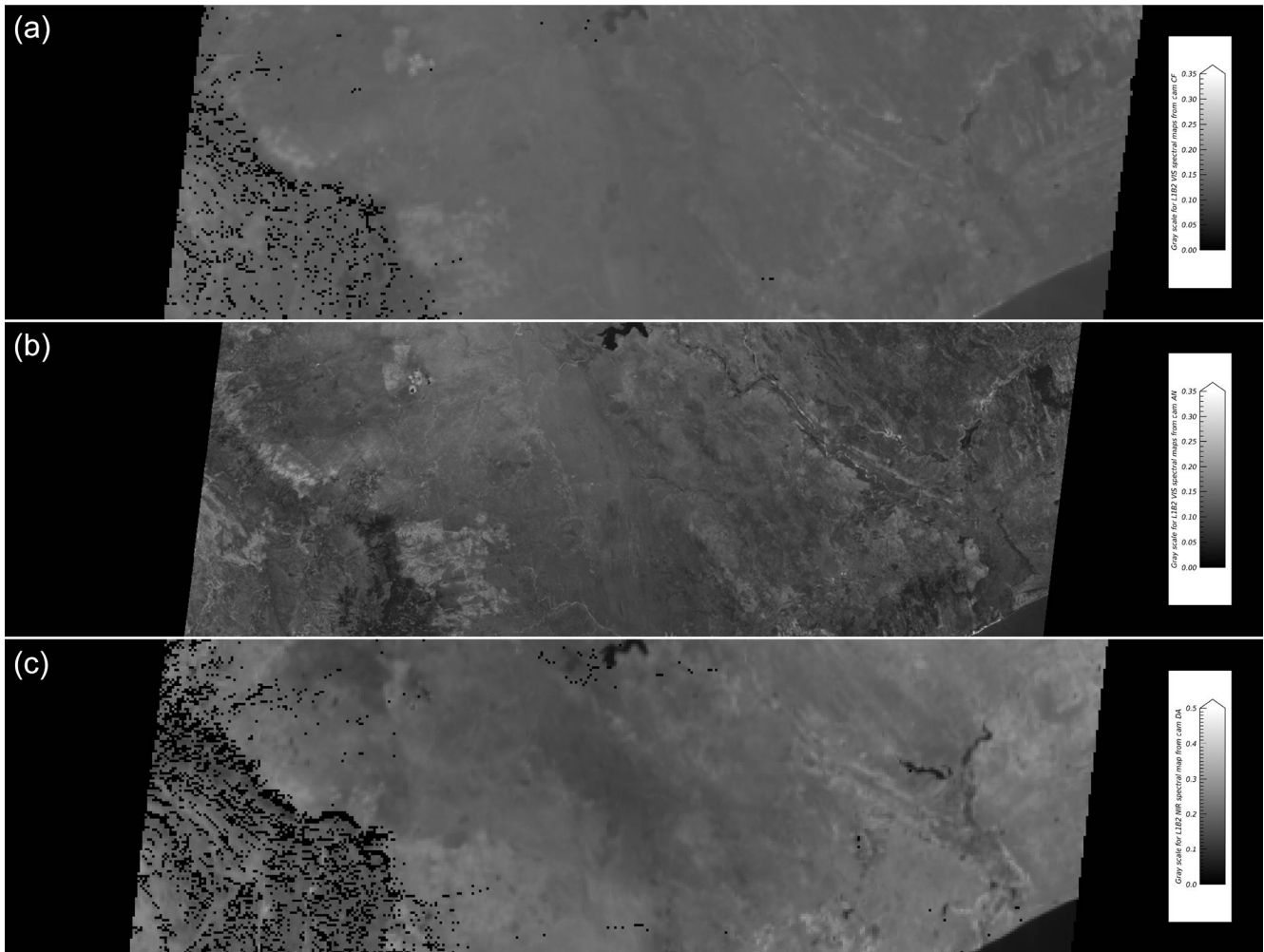
Figure 19. Maps of the MISR L1B2 data channels for the CF/green, AN/red and DA/NIR data channels of P168, O068050 and B110, where artificially inserted missing data have been replaced by best estimates using the algorithm described in this paper. The linear dimensions are the same as in Fig. 1, and gray scale stretching is the same as before: it assigns black to a null reflectance and white to reflectances of 0.35 or more in the blue, green and red spectral bands and 0.50 in the near-infrared spectral band.

6   Code and data availability

This paper describes version 2.2.0 of the L1B2 IDL functions available in the following GitHub repository: https://github.com/mmverstraete/MISR_L1B2 (last access: 12 March 2020); DOI: https://doi.org/10.5281/zenodo.3519988 (Verstraete, 2019b).

These functions in turn depend on more basic functions contained in separate repositories, listed here in order of increasing complexity:

– https://github.com/mmverstraete/Macros (last access: 12 March 2020),
  DOI: https://doi.org/10.5281/zenodo.3239995 (Verstraete, 2019e);

– https://github.com/mmverstraete/Utilities (last access: 12 March 2020),

  DOI: https://doi.org/10.5281/zenodo.3239999 (Verstraete, 2019f);

– https://github.com/mmverstraete/MISR_Tools (last access: 12 March 2020),
  DOI: https://doi.org/10.5281/zenodo.3240005 (Verstraete, 2019d);

– https://github.com/mmverstraete/MISR_AGP (last access: 12 March 2020),
  DOI: https://doi.org/10.5281/zenodo.3519897 (Verstraete, 2019a);

– https://github.com/mmverstraete/MISR_RCCM (last access: 12 March 2020),
  DOI: https://doi.org/10.5281/zenodo.3240017 (Verstraete, 2019c).

Each function contained in those repositories contains abundant in-line documentation to describe every processing step. An HTML file documenting each function in a standardized format is also available in each repository. Functions in the more elaborate repositories may depend on routines defined in more basic repositories. It is thus recommended to download and install the contents of all those repositories to have access to the full set of tools. Please remember also that those tools are under active development and may be updated in time.

The software code to update the RCCM data product further depends on additional external software resources as documented in Sect. 6 (Code availability) of Verstraete et al. (2020).

Lastly, for the benefit of users who may not have access to an IDL license, a license-free, self-contained, stand-alone, executable version of the software described above that uses the IDL Virtual Machine technology is available from the research data repository of GFZ Data Services (see Verstraete and Vogt, 2020; https://doi.org/10.5880/fidgeo.2020.011). A user manual describing the acquisition, installation and use of this software is also available from the same source.

All MISR data, including the RCCM and the L1B2 radiance data products mentioned in this paper, were obtained from the Atmospheric Science Data Center at the NASA Langley Research Center (LaRC). These data sets are openly available from the ASDC website at https://eosweb.larc.nasa.gov/project/misr/misr_table (last access: 12 March 2020). The references for those data sets are Diner et al. (1999b; http://doi.org/10.5067/Terra/MISR/MIRCCM_L2.004) for the RCCM and Jovanovic et al. (1999; http://doi.org/10.5067/Terra/MISR/MI1B2T_L1.003) for L1B2.

Two sets of resources have been made available on the research data repository of GFZ Data Services in conjunction with this paper. The first set (A; Verstraete et al., 2020; https://doi.org/10.5880/fidgeo.2020.012) includes five items: (A1) a compressed archive (L1B2_Out.zip) containing all intermediary, final and ancillary outputs created while generating the figures of this paper; (A2) a user manual (L1B2_Out.pdf) describing how to install, uncompress and explore those files; (A3) a compressed archive (L1B2_Suppl.zip) containing a similar set of additional results for eight other sites, spanning a much wider range of geographical, climatic and ecological conditions to show that the proposed algorithm works as well over areas other than southeastern Africa; (A4) a companion user manual (L1B2_Suppl.pdf) describing how to install, uncompress and explore those additional files; and (A5) a separate input MISR data archive (L1B2_input_68050.zip) for PATH 168, ORBIT 68050. This latter archive is usable with the second set (B; Verstraete and Vogt, 2020, https://doi.org/10.5880/fidgeo.2020.011), which includes (B1) a stand-alone, self-contained, executable version of the L1B2 correction codes (L1B2_Soft_Win.zip) that uses IDL Virtual Machine technology and does not re-

quire a paid IDL license as well as (B2) a user manual (L1B2_Soft_Win.pdf) that explains how to install, uncompress and use this software.

7 Conclusions

MISR's L1B2 Georectified Radiance Product (GRP) ellipsoid- or terrain-projected GLOBAL and LOCAL MODE files occasionally include missing or poor data values in one or more cameras, most often in several or all spectral bands. Their occurrence may result from multiple causes, but the most frequent is the switching between GLOBAL and LOCAL MODE. When a particular area is methodically acquired in LOCAL MODE, as is the case for the Skukuza site in Kruger National Park, South Africa, those BLOCKs are systematically contaminated by such missing data.

Every radiance measurement acquired by the MISR instrument is scaled to a 14-bit unsigned integer to which a 2-bit radiometric data quality indicator (RDQI) is then appended. Missing data are assigned a specific 16-bit scaled radiance code of 65523, equivalent to a 14-bit code of 16380 with an RDQI of 3 attached, while measurements of dubious value (e.g., possibly affected by sun glint) are identified with an RDQI of 2.

The process that generates these missing data points generally affects most or all of the four spectral bands but for only one or two (rarely three) of the nine cameras. However, due to the specific design of the instrument's focal planes, these missing lines affect different geographical locations in different spectral bands and cameras. Consequently, while a particular measurement may be missing in a given camera and spectral band, measurements may be available in other spectral bands or cameras for the same location at essentially the same time. The high correlation between some of the data channels then permits the estimation of those missing values.

A set of software functions, written in the IDL™ language, was developed to implement the algorithms described above and process MISR L1B2 GRP data to replace those missing values. A selection of cases was exhibited to visually show that the replacement process works well, and a series of tests based on the artificial insertion of missing data (in files that do not contain any) permitted us to quantitatively show the performance and accuracy of the procedure.

As an aside, radiance measurements rated as "poor", i.e., with an RDQI of 2, have often been found to cluster along those missing lines. These values could also optionally be replaced by estimates following the same procedure described above for missing data. The software allows this too, though in that case there is no obvious process for evaluating the results, i.e., there is no objective benchmark to decide whether the original value or the one suggested by the algorithm is closer to the nominal "true" value. The software does allow for the direct comparison between the original and the reconstructed values through statistics and scatterplots. Users can

experiment with both approaches and evaluate whether one or the other yields better or more appropriate results for their applications.

If missing or poor values are effectively replaced by estimates in the updated L1B2 data set, the RDQI assigned to the corrected scaled radiances in L1B2 data buffers is set to `1`.

The proposed method to replace missing and, optionally, poor data in MISR GLOBAL or LOCAL MODE files is generally applicable and has been implemented in the MISR-HR processing system. The materials in this paper are applicable to version 2.1.7 CE3 of the software unless noted explicitly in the in-line documentation of the IDL functions. All MISR L1B2 input files are available from NASA's LaRC ASDC Distributed Active Archive Center (DAAC), and routines to explore and address those issues are published on the first author's GitHub web page at https://github.com/mmverstraete (last access: 29 May 2020).

CE3: OK

Author contributions. MMV codeveloped the algorithm, ensured software testing and edited the initial and final draft of the manuscript; LAH was responsible for the codevelopment of the algorithm and updating the manuscript; VMJ contributed the detailed information on the origin of the missing data and the interpretation of the RDQI and commented on earlier drafts of the manuscript.

Competing interests. The authors declare that they have no conflict of interest.

Acknowledgements. The first two authors (Michel M. Verstraete and Linda A. Hunt) are greatly indebted to Bob Scholes (Global Change Institute, GCI, at the University of the Witwatersrand) for his unconditional scientific support for the MISR-HR project over the past decade and to Barend Erasmus, director of the GCI, for sponsoring yearly visits to South Africa during the period 2016–2019. Peter Vogt from the European Commission's Joint Research Centre (JRC) was instrumental in generating a self-contained, stand-alone, executable version of the L1B2 correction software based on IDL Virtual Machine technology. Hugo De Lemos from the GCI tested the IDL Virtual Machine package. The authors thank Sebastian Val from NASA Jet Propulsion Laboratory (JPL) for his support in maintaining and upgrading of the MISR Toolkit, an essential library to process MISR data product files. Last but not least, the first author (Michel M. Verstraete) thanks David J. Diner of JPL, principal investigator of the MISR instrument, for co-opting him into the MISR science team some 25 years ago and for his encouragement ever since.

Review statement. This paper was edited by Kirsten Elger and reviewed by two anonymous referees.

References

Armston, J. D., Scarth, P. F., Phinn, S. R., and Danaher, T. J.: Analysis of multi-date MISR measurements for forest and woodland communities, Queensland, Australia, Remote Sens. Environ., 107, 287–298, https://doi.org/10.1016/j.rse.2006.11.003, 2007.

Bull, M., Matthews, J., McDonald, D., Menzies, A., Moroney, C., Mueller, K., Paradise, S., and Smyth, M.: Data Products Specifications, Tech. Rep. JPL D-13963, Revision S, Jet Propulsion Laboratory, California Institute of Technology, Pasadena, CA, USA, availabe at: https://eosweb.larc.nasa.gov/project/misr/dps (last access: 29 May 2020), 2011.

Chopping, M., Moisen, G. G., Su, L., Laliberte, A., Rango, A., Martonchik, J. V., and Peters, D. P. C.: Large area mapping of southwestern forest crown cover, canopy height, and biomass using the NASA Multiangle Imaging Spectro-Radiometer, Remote Sens. Environ., 112, 2051–2063, https://doi.org/10.1016/j.rse.2007.07.024, 2008.

Diner, D. J., Bruegge, C. J., Martonchik, J. V., Ackerman, T. P., Davies, R., Gerstl, S. A. W., Gordon, H. R., Sellers, P. J., Clark, J., Daniels, J. A., Danielson, E. D., Duval, V. G., Klaasen, K. P., Lilienthal, G. W., Nakamoto, D. I., Pagano, R. J., and Reilly, T. H.: MISR: A Multiangle Imaging SpectroRadiometer for Geophysical and Climatological Research from EOS, IEEE T. Geosci. Remote, 27, 200–214, https://doi.org/10.1109/36.20299, 1989.

Diner, D. J., Beckert, J. C., Reilly, T. H., Ackerman, T. P., Bruegge, C. J., Conel, J. E., Davies, R., Gerstl, S. A. W., Gordon, H. R., Kahn, R. A., Martonchik, J. V., Muller, J.-P., Myneni, R. B., Pinty, B., Sellers, P. J., and Verstraete, M. M.: Multi-angle Imaging SpectroRadiometer (MISR) Instrument Description and Experiment Overview, IEEE T. Geosci. Remote, 36, 1072–1087, https://doi.org/10.1109/36.700992, 1998.

Diner, D. J., Asner, G. P., Davies, R., Knyazikhin, Y., Muller, J.-P., Nolin, A. W., Pinty, B., Schaaf, C. B., and Stroeve, J.: New Directions in Earth Observing: Scientific Applications of Multiangle Remote Sensing, B. Am. Meteorol. Soc., 80, 2209–2228, https://doi.org/10.1175/1520-0477(1999)080<2209:NDIEOS>2.0.CO;2, 1999a.

Diner, D. J., Di Girolamo, L., and Clothiaux, E. E.: Level 1 Cloud Detection Algorithm Theoretical Basis, Tech. Rep. JPL D-13397, Revision B, Jet Propulsion Laboratory, California Institute of Technology, Pasadena, CA, USA, https://doi.org/10.5067/Terra/MISR/MIRCCM_L2.004, 1999b.

Diner, D. J., Verstraete, M. M., and Martonchik, J. V.: Foreword to Special Section on MISR, IEEE T. Geosci. Remote, 40, 1447–1448, https://doi.org/10.1109/TGRS.2002.802777, 2002.

Diner, D. J., Braswell, B. H., Davies, R., Gobron, N., Hu, J., Jin, Y., Kahn, R. A., Knyazikhin, Y., Loeb, N., Muller, J.-P., Nolin, A. W., Pinty, B., Schaaf, C. B., Seiz, G., and Stroeve, J.: The value of multiangle measurements for retrieving structurally and radiatively consistent properties of clouds, aerosols, and surfaces, Remote Sens. Environ., 97, 495–518, https://doi.org/10.1016/j.rse.2005.06.006, 2005.

Jovanovic, V. M., Lewicki, S. A., Smyth, M. M., Zong, J., and Korechoff, R. P.: Level 1 Georectification and Registration Algorithm Theoretical Basis, Tech. Rep. JPL D-11532, Revision D, Jet Propulsion Laboratory, California Institute of Technology, Pasadena, CA, USA, https://doi.org/10.5067/Terra/MISR/MI1B2T_L1.003, 1999.

Liu, Z., Verstraete, M. M., and de Jager, G.: Handling outliers in model inversion studies: a remote sensing case study using MISR-HR data in South Africa, S. Afr. Geogr. J., 100, 122–139, https://doi.org/10.1080/03736245.2017.1339629, 2018.

Mahlangu, P., Mathieu, R., Wessels, K., Naidoo, L., Verstraete, M. M., Asner, G., and Main, R.: Indirect Estimation of Structural Parameters in South African Forests Using MISR-HR and LiDAR Remote Sensing Data, Remote Sens., 10, 1537–1567, https://doi.org/10.3390/rs10101537, 2018.

Pisek, J. and Chen, J. M.: Mapping forest background refectivity over North America with Multi-angle Imaging SpectroRadiometer (MISR) data, Remote Sens. Environ., 113, 2412–2423, https://doi.org/10.1016/j.rse.2009.07.003, 2009.

Van den Hoof, C., Verstraete, M. M., and Scholes, R. J.: Differing Responses to Rainfall Suggest More Than One Functional Type of Grassland in South Africa, Remote Sens., 10, 2055–2077, https://doi.org/10.3390/rs10122055, 2018.

Verstraete, M. M.: mmverstraete/MISR_AGP: IDL MISR_AGP Version 2.1.0., https://doi.org/10.5281/3240011, 2019a.

Verstraete, M. M.: mmverstraete/MISR_L1B2: IDL MISR_L1B2 Version 2.2.0., https://doi.org/10.5281/zenodo.3519988, 2019b.

Verstraete, M. M.: mmverstraete/MISR_RCCM: IDL MISR_RCCM Version 2.2.0, https://doi.org/10.5281/zenodo.3240017, 2019c.

Verstraete, M. M.: mmverstraete/MISR_Tools: IDL MISR_Tools Version 2.1.0., https://doi.org/10.5281/zenodo.3240005, 2019d.

Verstraete, M. M.: mmverstraete/Macros: IDL Macros Version 2.1.0., https://doi.org/10.5281/zenodo.3239995, 2019e.

Verstraete, M. M.: mmverstraete/Utilities: IDL Utilities Version 2.1.0, https://doi.org/10.5281/zenodo.3239999, 2019f.

Verstraete, M. M., Hunt, L. A., Scholes, R. J., Clerici, M., Pinty, B., and Nelson, D. L.: Generating 275-m Resolution Land Surface Products From the Multi-Angle Imaging SpectroRadiometer Data, IEEE T. Geosci. Remote, 50, 3980–3990, https://doi.org/10.1109/TGRS.2012.2189575, 2012.

Verstraete, M. M., Hunt, L. A., De Lemos, H., and Di Girolamo, L.: Replacing missing values in the standard Multi-angle Imaging SpectroRadiometer (MISR) radiometric camera-by-camera cloud mask (RCCM) data product, Earth Syst. Sci. Data, 12, 611–628, https://doi.org/10.5194/essd-12-611-2020, 2020.

Wei, S. and Fang, H.: Estimation of canopy clumping index from MISR and MODIS sensors using the normalized difference hotspot and darkspot (NDHD) method: The influence of BRDF models and solar zenith angle, Remote Sens. Environ., 187, 476–491, https://doi.org/10.1016/j.rse.2016.10.039, 2016.

Yang, Y., Di Girolamo, L., and Mazzoni, D.: Selection of the automated thresholding algorithm for the Multi-angle Imaging SpectroRadiometer Radiometric Camera-by-Camera Cloud Mask over land, Remote Sens. Environ., 107, 159–171, https://doi.org/10.1016/j.rse.2006.05.020, 2007.

Zhao, G. and Di Girolamo, L.: A cloud fraction versus view angle technique for automatic in-scene evaluation of the MISR cloud mask, J. Appl. Meteorol., 43, 860–869, https://doi.org/10.1175/1520-0450(2004)043<0860:ACFVVA>2.0.CO;2, 2004.

Remarks from the language copy-editor

Remarks from the typesetter